Monthly Notices
of the
ROYAL ASTRONOMICAL SOCIETY

MNRAS **488,** 2629–2643 (2019)
Advance Access publication 2019 July 10

doi:10.1093/mnras/stz1887

Radiative properties of the first galaxies: rapid transition between UV and infrared bright phases

Shohei Arata [1]★ Hidenobu Yajima,[2] Kentaro Nagamine [1,3,4] Yuexing Li[5,6] and Sadegh Khochfar[7]

[1]*Theoretical Astrophysics, Department of Earth and Space Science, Graduate School of Science, Osaka University, Toyonaka, Osaka 560-0043, Japan*
[2]*Center of Computational Sciences, University of Tsukuba, Ibaraki 305-8577, Japan*
[3]*Department of Physics & Astronomy, University of Nevada, Las Vegas, 4505 S. Maryland Pkwy, Las Vegas, NV 89154-4002, USA*
[4]*Kavli IPMU (WPI), The University of Tokyo, 5-1-5 Kashiwanoha, Kashiwa, Chiba 277-8583, Japan*
[5]*Department of Astronomy & Astrophysics, The Pennsylvania State University, 525 Davey Lab, University Park, PA 16802, USA*
[6]*Institute for Gravitation and the Cosmos, The Pennsylvania State University, University Park, PA 16802, USA*
[7]*SUPA, Institute for Astronomy, University of Edinburgh, Royal Observatory, Edinburgh EH9 3HJ, UK*

Accepted 2019 June 24. Received 2019 June 23; in original form 2018 October 17

ABSTRACT

Recent observations have successfully detected UV-bright and infrared-bright galaxies in the epoch of reionization. However, the origin of their radiative properties has not been understood yet. Combining cosmological hydrodynamic simulations and radiative transfer calculations, we present predictions of multiwavelength radiative properties of the first galaxies at $z \sim 6$–15. Using zoom-in initial conditions, we investigate three massive galaxies and their satellites in different environment and halo masses at $z = 6$: $M_{\rm h} = 2.4 \times 10^{10}$, 1.6×10^{11}, and $0.7 \times 10^{12}\,{\rm M}_{\odot}$. We find that most of the gas and dust are ejected from star-forming regions by supernova feedback, which allows the UV photons to escape. We show that the peak of the spectral energy distribution (SED) rapidly changes between UV and infrared wavelengths on a time-scale of ~ 100 Myr due to intermittent star formation and feedback, and the escape fraction of UV photons fluctuates in the range of 0.2–0.8 at $z < 10$ with a time-averaged value of 0.3. When dusty gas covers the star-forming regions, the galaxies become bright in the observed-frame sub-millimeter wavelengths. We predict the detectability of high-z galaxies with the Atacama Large Millimeter Array (ALMA). For a sensitivity limit of 0.1 mJy at 850 μm, the detection probability of galaxies in haloes $M_{\rm h} \gtrsim 10^{11}\,{\rm M}_{\odot}$ at $z \lesssim 7$ exceeds fifty per cent. We argue that supernova feedback can produce the observed diversity of SEDs for high-z galaxies.

Key words: hydrodynamics – radiative transfer – galaxies: evolution – galaxies: formation – galaxies: high-redshift – galaxies: ISM.

1 INTRODUCTION

Understanding galaxy evolution is one of the main goals of modern astronomy and astrophysics. Recent observations have detected many galaxies in the early Universe, the so-called *first galaxies*, in the optical and near-infrared wavelengths (e.g. Ouchi et al. 2009; Ono et al. 2012; Shibuya et al. 2012; Finkelstein et al. 2013, 2015; McLure et al. 2013; Bouwens et al. 2015; Oesch et al. 2016; Bowler et al. 2018; Ono et al. 2018), or in the sub-millimeter wavelengths (Riechers et al. 2013; Watson et al. 2015; Inoue et al. 2016; Hashimoto et al. 2018; Marrone et al. 2018).

In observational studies of high-z galaxies, a large number of star-forming galaxies are usually colour-selected first as Lyman-break galaxies (LBGs; e.g. Steidel et al. 1996, 2003; Shapley et al. 2003; Bouwens et al. 2015; Oesch et al. 2016; Bowler et al. 2018), and then later their redshifts are confirmed by spectroscopy. Many high-z galaxies at $z \gtrsim 6$ are also detected by the Lyα line (LAEs; e.g. Ouchi et al. 2003; Dawson et al. 2004; Hu et al. 2004; Kashikawa et al. 2006; Shimasaku et al. 2006; Gronwall et al. 2007; Ouchi et al. 2009, 2010). In addition, Atacama Large Millimeter Array (ALMA) observations are beginning to provide valuable information on high-z galaxies via detections of dust continuum, metal lines, and molecular lines (e.g. Inoue et al. 2016; Hashimoto et al. 2019), so-called sub-millimeter galaxies (SMGs; Marrone et al. 2018). For example, Riechers et al. (2013) showed that the dusty massive starburst galaxies are already formed as early as at $z \sim 6$. These different varieties of high-z population and radiative properties probably reflect different physical conditions in the first galaxies. Therefore studying the radiative output from the first galaxies

★ E-mail: arata@astro-osaka.jp

is one of the primary ways to understand galaxy formation and evolution.

The formation mechanism of the first galaxies has been studied by numerical simulations (Greif et al. 2008; Maio et al. 2011; Safranek-Shrader et al. 2012; Wise et al. 2012; Johnson, Dalla Vecchia & Khochfar 2013; Hopkins et al. 2014; Kimm & Cen 2014; Paardekooper, Khochfar & Dalla Vecchia 2015; Yajima et al. 2015a,b; Ricotti, Parry & Gnedin 2016; Trebitsch et al. 2017; Yajima et al. 2017a; Kim et al. 2018). These studies reveal that stellar and supernova (SN) feedback are crucial for galaxy evolution. In particular, Yajima et al. (2017a) studied galaxy evolution in massive haloes ($M_{\rm h} \gtrsim 10^{11}$ M$_\odot$) at $z \gtrsim 6$ using cosmological hydrodynamic simulations, and found that the star formation occurs intermittently due to SN feedback and gas accretion (see also Kimm & Cen 2014). However, the radiative properties associated with the bursty star formation history are not fully understood yet. In this paper, we focus on the radiative output of the first galaxies by carrying out radiative transfer calculations in post-processing of zoom-in cosmological hydrodynamic simulations.

Earlier work studying the radiative properties of the first galaxies with similar methodologies include e.g. Yajima et al. (2015b) who found that simulated galaxies in 5σ overdense regions were heavily obscured by dust, and bright at infrared wavelengths. Wilkins et al. (2016) investigated the statistical nature of the first galaxies using the galaxy sample in a cosmological volume of $(577\,{\rm cMpc})^3$, and successfully reproduced the observed UV luminosity function and the stellar mass function. They showed that the stellar radiation from massive galaxies suffered from dust extinction even at $z \sim 8$. These previous studies suggest that galaxies smoothly evolved into a dust-obscured state as the halo mass increases. Dust extinction might even reduce observability of galaxies at redshifts as large as $z \sim 15$ (Barrow et al. 2018).

Recent high-resolution simulations with state-of-the-art SN feedback models showed that the star formation rate (SFR) and gas structure change rapidly on short time-scales due to galactic outflows (Davis, Khochfar & Dalla Vecchia 2014; Hopkins et al. 2014; Kimm & Cen 2014; Yajima et al. 2017a). Thus, strong galactic outflows are likely to change the radiative properties of galaxies as well. However, it has not been understood well how intense starbursts change the relation between radiative properties of galaxies and their evolution. Ma et al. (2015) investigated the escape fraction of ionizing photons in less-massive galaxies ($M_{\rm h} \sim 10^9$–10^{11} M$_\odot$), and showed that it was significantly affected by intermittent star formation (see also, Paardekooper et al. 2015). Yajima et al. (2017a) suggested that even massive galaxies with $M_{\rm h} \gtrsim 10^{11}$ M$_\odot$ experience short starbursts, and high-density dusty gas occupies the star-forming regions at Galactic Centres until outflow are launched. Despite progress in our understanding on feedback, the radiative properties of massive galaxies are still unclear. We here focus on the radiative properties of massive galaxies which go through repeated short starbursts and investigate their relation to the origin of observed SMGs.

In order to study the radiative properties, we need to know the spatial distribution of dust and stars. As galaxies evolve, dust and metals are produced via Type II SNe.[1] When the interstellar dust absorbs the stellar UV radiation and re-emits the energy in the infrared, the galaxy can be bright in the sub-mm wavelengths due to the thermal emission from dust. In contrast, if the dust absorption is ineffective, star-forming galaxies are bright in the rest-frame UV wavelengths and become targets for Hubble Space Telescope (HST), Subaru, and Keck telescopes.

Dust attenuation sensitively depends on the dust abundance, size distribution, and spatial distribution. However, the information on the dust properties from observations is limited, and theoretical studies can give important insight. For example, Todini & Ferrara (2001) theoretically studied the dust size and composition by taking into account the dust growth/destruction processes in SN shock (see also, Schneider et al. 2006; Nozawa et al. 2007; Chiaki, Yoshida & Kitayama 2013; Chiaki et al. 2015). Asano et al. (2013) evaluated the dust properties using phenomenological models which considered dust formation and destruction processes in combination with star formation histories in galaxies. Yajima et al. (2014b) carried out radiative transfer calculations in cosmological simulations, and estimated the typical dust size by comparing the colours of simulated galaxies and observations. Cullen et al. (2017) examined the dust attenuation law by matching the UV-LF and UV-beta slope of simulated galaxies, and showed that the Calzetti law is actually the best description rather than the SMC law (see also, Cullen et al. 2018). More recently, Narayanan et al. (2018) showed that the dust extinction curve varied due to the inhomogeneous spatial distribution of dust for star-forming galaxies at $z = 0$–6 in cosmological simulations (see also, Hou et al. 2017). In addition, Behrens et al. (2018) studied the temperature and amount of dust in the observed SMG at $z = 8.38$ (Laporte et al. 2017) using cosmological simulations. In this work, we study the sub-mm fluxes from more massive galaxies with bursty star formation histories and the impact of stellar feedback on the radiative properties of first galaxies at $z \gtrsim 6$ using cosmological zoom-in hydrodynamic simulations.

In addition to the spectral energy distribution (SED) of galaxies, the size of galaxies at UV wavelengths is likely to change as galaxies evolve. Galaxy sizes have a large impact on the observational estimation of the faint-end slope of UV luminosity function, because of surface brightness dimming and observational limits (Grazian et al. 2011). As we discuss in this paper, the morphology and the extension of galactic disc is significantly dependent on the feedback strength at high-z, and if the extended low-mass galaxies are missed in the current Hubble Frontier Fields observation, the cosmic SFRD could be significantly underestimated at $z \gtrsim 6$ (e.g. Jaacks et al. 2012a). The low-mass galaxies studied in this paper are mainly satellites of massive galaxies at $z \gtrsim 6$, and separate zoom simulations of low-density regions will have to be performed in the future to examine the low-mass galaxies in the field regions (e.g. Ma et al. 2018a). In any case, we investigate the galaxy sizes as well as SEDs by radiative transfer calculations, and find an interesting transition between UV to sub-mm bright phase due to intermittent starburst and its feedback. This fluctuation may affect the estimate of luminosity function as we will discuss in Section 3.3, and we quantify the duty cycle of such fluctuations.

Our paper is organized as follows. We describe the methodologies of cosmological hydrodynamic simulations and radiative transfer calculations in Section 2. In Section 3, we present our results. In

[1] AGB stars also produce dust. However, the evolution of low-mass stars towards the AGB phase takes longer than 1 Gyr. Thus, SNe dominate the dust enrichment of first galaxies, which occurs at the end of the lifetimes of massive stars ($\lesssim$10 Myr). The pair-instability SNe are also important in the early universe (e.g. Nozawa et al. 2007), but for evolved galaxies Type-II SNe dominate the dust production. For example, Maiolino et al. (2004) showed that the extinction curves of $z \sim 6$ quasars agree with the Type II SN model.

Table 1. Parameters of our zoom-in cosmological hydrodynamic simulations: (1) $M_{\rm h}$ is the halo mass at $z = 6$. (2) $m_{\rm DM}$ is the mass of a dark matter particle. (3) $m_{\rm gas}$ is the initial mass of a gas particle. (4) $\epsilon_{\rm min}$ is the gravitational softening length in comoving units. (5) A is the amplitude factor for the star formation model based on the Kennicutt–Schmidt law (Schaye & Dalla Vecchia 2008). The Halo-11-lowSF and Halo-12-lowSF runs have a lower star formation amplitude factor. The Halo-11-noSN and Halo-12-noSN runs have no SN feedback. We refer to the Halo-11 and Halo-12 as the *fiducial* runs.

Halo ID	$M_{\rm h}$ (h^{-1} M$_\odot$)	$m_{\rm DM}$ (h^{-1} M$_\odot$)	$m_{\rm gas}$ (h^{-1} M$_\odot$)	$\epsilon_{\rm min}$ (h^{-1} pc)	SNe feedback	A
Halo-10	2.4×10^{10}	6.6×10^{4}	1.2×10^{4}	200	ON	2.5×10^{-3}
Halo-11	1.6×10^{11}	6.6×10^{4}	1.2×10^{4}	200	ON	2.5×10^{-3}
Halo-12	7.5×10^{11}	1.1×10^{6}	1.8×10^{5}	200	ON	2.5×10^{-3}
Halo-11-lowSF	1.6×10^{11}	6.6×10^{4}	1.2×10^{4}	200	ON	2.5×10^{-4}
Halo-11-noSN	1.6×10^{11}	6.6×10^{4}	1.2×10^{4}	200	OFF	2.5×10^{-3}
Halo-12-lowSF	7.5×10^{11}	1.1×10^{6}	1.8×10^{5}	200	ON	2.5×10^{-4}
Halo-12-noSN	7.5×10^{11}	1.1×10^{6}	1.8×10^{5}	200	OFF	2.5×10^{-3}

Sections 3.1 and 3.3, we focus on the fluctuation of UV escape fraction and sub-mm flux of dust re-emission, respectively. In Section 3.4, we present the detectability of first galaxies by ALMA. In Sections 3.5 and 3.6, we show the dust temperature and half-light radius of galaxies at UV wavelength. In addition, we discuss the dependence of our results on the models of star formation and feedback in Section 4. Finally we summarize our main conclusions in Section 5.

2 METHOD

2.1 Cosmological hydrodynamic simulations

We use the same zoom-in cosmological hydrodynamic simulation as in Yajima et al. (2017a, hereafter Y17), who focused on three haloes in different environment with halo masses $2.4 \times 10^{10}\ h^{-1}\,{\rm M}_\odot$ (Halo-10), $1.6 \times 10^{11}\ h^{-1}\,{\rm M}_\odot$ (Halo-11), and $7.5 \times 10^{11}\ h^{-1}\,{\rm M}_\odot$ (Halo-12) at $z = 6$. The simulations were carried out with the smoothed particle hydrodynamics (SPH) code GADGET-3 (Springel 2005) with the subgrid models developed in *Overwhelmingly Large Simulations* (OWLS) project (Schaye et al. 2010) and the *First Billion Year* (FiBY) project (e.g. Johnson et al. 2013) which reproduce the general properties of the high-redshift galaxy population well (e.g. Cullen et al. 2017).

The local SFR in the simulations is estimated via local pressure:

$$\dot{m}_* = m_{\rm g} A (1\ {\rm M}_\odot\ {\rm pc}^{-2})^{-n} \left(\frac{\gamma}{G} f_{\rm g} P\right)^{(n-1)/2}, \quad (1)$$

where A and n are the tuning parameters, $m_{\rm g}$ is the initial mass of gas particles, $\gamma = 5/3$ is the ratio of specific heats, $f_{\rm g}$ is the gas mass fraction in the self-gravitating galactic disc, and P is the total interstellar medium (ISM) pressure. We set $f_{\rm g} = 1$ and the threshold density for star formation as $n_{\rm th} = 10\,{\rm cm}^{-3}$. This star formation model was originally derived in Schaye & Dalla Vecchia (2008) and is based on the Kennicutt–Schmidt law of local galaxies, $\dot{\Sigma}_* = A(\frac{\Sigma_{\rm gas}}{1\ {\rm M}_\odot\ {\rm pc}^{-2}})^n$(e.g. Kennicutt 1998). In this work, we adopt $A = 2.5 \times 10^{-3}$ M$_\odot$ yr^{-1} kpc^{-2} and $n = 1.4$ in the fiducial runs. Our choice of the parameter A is higher than observed in local galaxies. However, recent observations of merging or high-z galaxies suggested that the parameter A tends to be higher than for local galaxies (e.g. Genzel et al. 2010; Tacconi et al. 2013). As a comparison and to gauge the importance of this choice, we also investigate the additional simulation with $A = 2.5 \times 10^{-4}$ M$_\odot$ yr^{-1} kpc^{-2} (Halo-11-lowSF) which is similar to the value found in local galaxies.

For SN feedback, we inject thermal energy into neighbour gas particles stochastically (Dalla Vecchia & Schaye 2012), and the gas temperature is increased to $10^{7.5}$ K. The thermal energy is efficiently converted to kinetic energy against radiative cooling loss, if the gas density is lower than the critical value of $n_{\rm H} \sim 100\ {\rm cm}^{-3}\ (T/10^{7.5}\,{\rm K})(m_{\rm g}/10^4\,{\rm M}_\odot)^{-1/2}$, where $m_{\rm g}$ is the mass of a gas particle. The numerical resolution of our simulations successfully capture galactic winds and suppress star formation (see Y17).

The volumes of the entire simulation boxes are $(20\,h^{-1}\,{\rm Mpc})^3$ for Halo-10 and Halo-11, and $(100\,h^{-1}\,{\rm Mpc})^3$ for Halo-12 in comoving units. In order to increase the resolution, Y17 used the zoom-in initial conditions for the regions of $(1-2\ h^{-1}\,{\rm Mpc})^3$ for Halo-10 and Halo-11 and $(6.6\ h^{-1}\,{\rm Mpc})^3$ for Halo-12, which achieved the resolution of $\sim$10–30 pc in physical units at $z \sim 10$. With this resolution, the ISM structure within galaxies are resolved down to the scales of just above molecular clouds, and the results of our radiative transfer calculation is more reliable than those using cosmological simulations with resolution coarser than 100 pc as we describe in the next subsection. Other parameters are shown in Table 1.

The upper panels of Fig. 1 show the distribution of gas, stars, and dust in Halo-11 at $z \sim 6$. We calculate the dust amount from gas metallicity (see Section 2.2). In our simulations, we use the star formation model based on Kennicutt–Schmidt law (Schaye & Dalla Vecchia 2008) and the stochastic thermal feedback model for SN feedback (Dalla Vecchia & Schaye 2012). For Halo-10, Halo-11, and Halo-12 runs, we use the same parameter set for star formation and feedback models, and we refer them as *fiducial* case. Y17 also compared the evolution of Halo-11 in the case of lower star formation efficiency (Halo-11-lowSF) and the case without SN feedback (Halo-11-noSN). We further add the Halo-12-lowSF and Halo-12-noSN runs to evaluate the impact of subgrid models on the radiative properties. We examine the radiative properties of first galaxies in these different haloes in Section 4.

2.2 Radiative transfer

We use the radiative transfer code, All-wavelength Radiative Transfer with Adaptive Refinement Tree (ART^2: Li et al. 2008; Yajima, Choi & Nagamine 2012). Here we briefly explain the features of the code.

ART^2 is based on a Monte Carlo technique. It tracks the propagation of photon packets emitted from star particles, and computes the emergent SED of a galaxy. The intrinsic SED of each star particle before dust extinction is calculated by STARBURST99 with the information of stellar age and metallicity. We assume the Chabrier IMF with the mass range from 0.1 to 100 M$_\odot$ (Chabrier 2003). For each galaxy, we cast 10^6 photon packets, which is sufficient to achieve a reasonable convergence, based on the comparison with

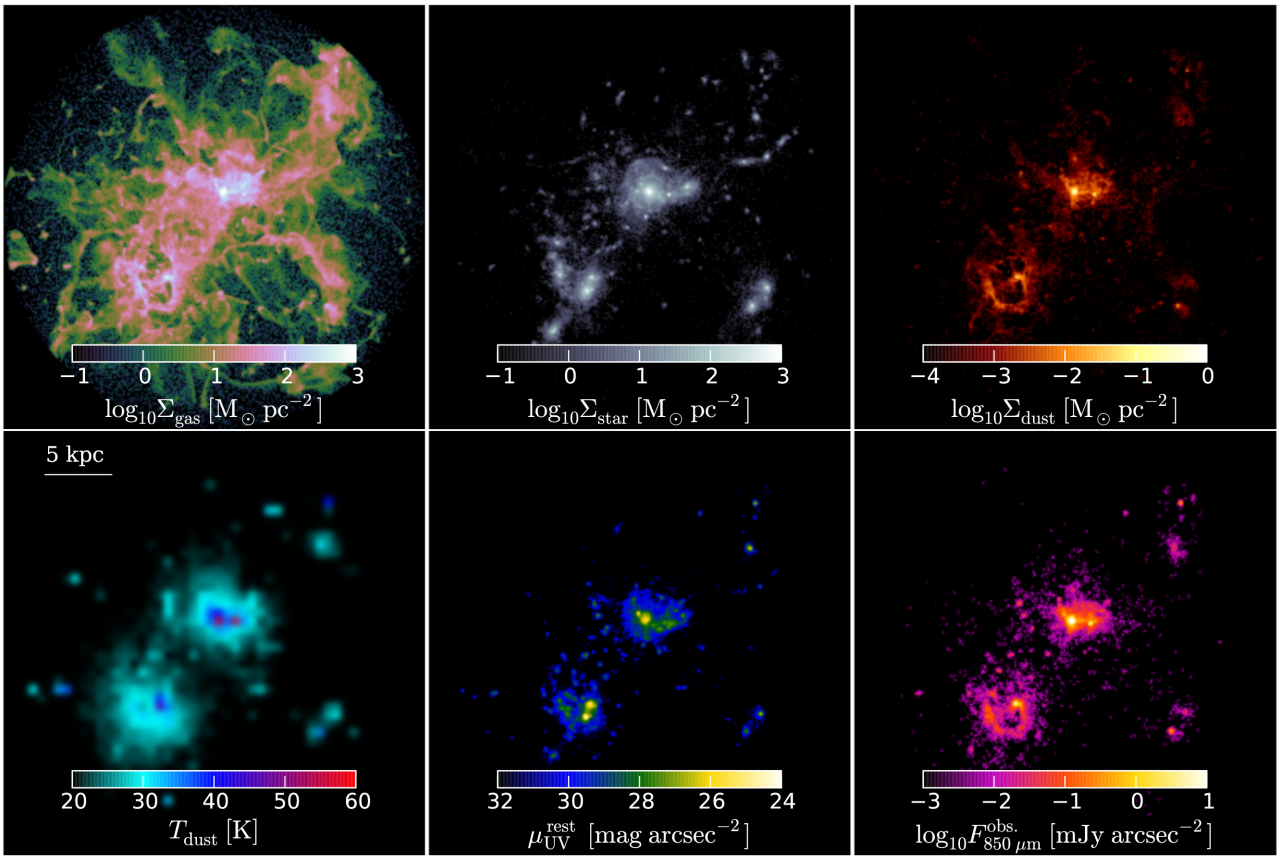

Figure 1. Maps of the main galaxy in Halo-11 run at $z \sim 6$. *Top panels:* Column density of gas (left), stars (middle), and dust (right). *Bottom panels:* Dust temperature (left), surface brightness of the rest-frame UV continuum (middle), and the observed-frame sub-mm continuum (right). The pixel size is ∼0.02 arcsec. The spatial scale of 5 kpc (physical) is displayed in the bottom left panel.

the case of 10^5 photon packets. ART^2 uses an adaptive refinement grid structure. We initially construct 4^3 base grid over the zoom region which covers twice the size of virial radius. If the number of SPH particles in a cell is greater than 16, the cell is further refined by 2^3 grid. We set the maximum refinement level to 12 which achieves the resolution of 2.7 h^{-1} pc for Halo-11 at $z = 6$.

Even in the current resolution, it is difficult to resolve the multiphase ISM accurately. Thermal instability is one of the main processes to form multiphase ISM (e.g. Field 1965; McKee & Ostriker 1977), and it can occur even in the high-z galaxies with low metallicities (e.g. Inoue & Omukai 2015). Arata, Yajima & Nagamine (2018) found that the spatial resolution of $\lesssim$0.01 pc was required to follow the formation of dense cold clumps, which is still difficult to achieve even with the state-of-the-art cosmological zoom simulations. Therefore, ART^2 calculates the radiative transfer with a subgrid multiphase ISM model based on Springel & Hernquist (2003), which computes the density of cold dense clouds within the hot phase assuming pressure equilibrium. In our multiphase model, we assume that the cold phase consists of randomly distributed molecular clouds which follow the observed power-law mass distribution of giant molecular clouds ($\mathrm{d}n/\mathrm{d}M \propto M^{-2}$, e.g. Andre, Ward-Thompson & Motte 1996), and the mass–size relation ($M \propto R^2$, e.g. Solomon et al. 1987). The physical properties such as density and volume filling factor of the cold phase are derived from the hydrodynamic cosmological simulations. The propagation of photons in the multiphase ISM is calculated by statistically sampling these clouds in the ray tracing process. (see Li et al. 2008 for more details).

We assume that the dust-to-gas mass ratio $\mathcal{D}$ in the cold clouds is proportional to the local metallicity as in the local galaxies, $\mathcal{D} = 8 \times 10^{-3}\ (Z/Z_\odot)$ (Draine et al. 2007). On the other hand, $\mathcal{D}$ in the hot gas is scaled by the hydrogen neutral fraction considering that the dust is efficiently destroyed in the ionized regions. When the ionized gas recombines, it is split into two phases again. For example, in a cold cloud with $n_{\rm H} = 10^3$ cm^{-3} and $T = 50$ K, the time-scale of dust growth via accretion is $\sim 10(Z/0.1Z_\odot)$ Myr (Hirashita & Kuo 2011), which roughly corresponds to the time interval between our snapshots. Thus the dust reformation proceeds fast enough, and the total dust mass is dominated by the dust in the cold clouds.

We adopt the dust size distribution of Todini & Ferrara (2001) for solar metallicity and $M = 22$ $\rm M_\odot$ SN model. The dust opacity curve is calculated by combining the size distribution with the cross-section of Weingartner & Draine (2001).

To obtain panchromatic SEDs, ART^2 treats the transfer of photons with various frequencies. First, it tracks the propagation of ionizing photons. Then, using the obtained ionized structure, it calculates the transfer of UV continuum and dust absorption/re-emission. When the dust absorbs photon packets within a time interval Δt, the dust temperature is updated under the assumption of radiative

equilibrium:

$$E_{\rm abs} = 4\pi\,\Delta t\,\kappa_{\rm P}(T_{\rm d})\,B(T_{\rm d})\,m_{\rm d}, \quad (2)$$

where $\kappa_{\rm P} = \int \kappa_\nu B_\nu {\rm d}\nu / \int B_\nu {\rm d}\nu$ is the Planck mean opacity, and B_ν is the blackbody radiation. After the determination of dust temperature, we calculate the radiative transfer of infrared photons from dust.

3 RESULT

3.1 Projected images

Fig. 1 shows various projection plots of Halo-11 at $z = 6$ including UV and sub-mm surface brightness. The total stellar mass, gas mass, and dust mass in this halo are $M_\star = 2.4 \times 10^9\,h^{-1}\,{\rm M}_\odot$, $M_{\rm gas} = 2.5 \times 10^{10}\,h^{-1}\,{\rm M}_\odot$, and $M_{\rm dust} = 2 \times 10^7\,h^{-1}\,{\rm M}_\odot$.

The top left panel shows the total gas column density, which is extended over about 20 kpc (physical) with complex filamentary structure. The gas distribution is disturbed by multiple galaxy mergers and high gas inflow rate, and its motion is turbulent. The green, pink, and white regions correspond to hydrogen column densities of $N_{\rm H} \sim 10^{20}, 10^{21}, 10^{22}\,{\rm cm}^{-2}$, respectively. The pink and white regions would certainly correspond to damped Lyα systems (DLAs), which will produce a deep absorption trough if we were to have a bright quasar behind this system as a background source.

The top middle panel shows a massive stellar system in the centre of this halo with $M_\star \sim 10^9 h^{-1}\,{\rm M}_\odot$, and there is another relatively large satellite galaxy in the lower left side of the panel with $M_\star \sim 3 \times 10^8 h^{-1}\,{\rm M}_\odot$ which will soon merge with the central system, where we identify satellite galaxies with SUBFIND algorithm (Springel et al. 2001). The middle bottom panel shows the UV surface brightness, which traces the young stellar population. Here, the brightest white pixels have $m_{\rm AB} \sim 24.1$ mag arcsec^{-2}, corresponding to the local projected SFR of about 49 ${\rm M}_\odot\,{\rm yr}^{-1}\,{\rm arcsec}^{-2}$.

The top right panel shows the projected dust mass distribution, which largely traces the stellar distribution, but with interesting offsets on small scales. The observed sub-mm surface brightness reflects the underlying dust distribution, and 850 μm surface brightness is shown in the bottom right panel. Here, the brightest pixel has 0.84 mJy arcsec^{-2}, and most of the UV radiation are absorbed by dust in such a region. The brightest pixel of observed sub-mm band is in the main galaxy, meanwhile that of rest-UV band is in the satellite galaxy on the lower left side of the panel, resulting in a large offset of ~ 1.4 arcsec between them, which corresponds to a physical separation of 8 kpc at $z = 6$. Such an offset has been discovered in the observed galaxies at $z \sim 7$ (Bowler et al. 2018; Hashimoto et al. 2019). This suggests that some star-forming regions are obscured by dust, while others are optically thin to the UV radiation.

In the right-column panels, there is also an interesting bubble-like structure around the satellite galaxy on the lower left side of the panel, which presumably was caused by the SN feedback from nearby starburst. We will study the dynamics of these SN bubbles in the future furthermore.

3.2 SFR and escape fraction

The top and second panels of Fig. 2 show the redshift evolution of SFR and gas density at the Galactic Centre of Halo-11 at $z =$ 6–15. Since Y17 already discussed them, here we explain only the important points briefly. The figure shows the intermittent star formation of Halo-11, which is driven by the cycle of following processes: (1) the central density increases as the gas is accreted due to the gravitational force of the halo, which drives active star formation; (2) at the end of the lifetime of massive stars ($\sim$10 Myr), Type II SNe occur, and the galactic wind is launched, resulting in the quenching of star formation.

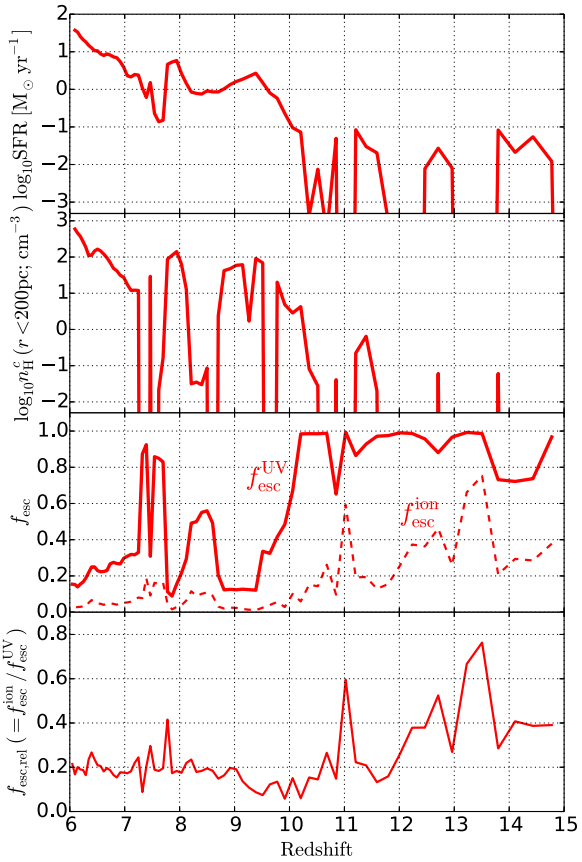

Figure 2. Redshift evolution of SFR (top panel), mean gas density within 200 pc from the Galactic Centre (second panel). The third panel shows the absolute escape fraction for our fiducial run (Halo-11), where solid and dashed lines represent UV continuum (1500–2800 Å) and Lyman-continuum photons ($\leq$912 Å), respectively. The bottom panel shows the relative escape fraction as defined in the main text.

The third panel of Fig. 2 shows the evolution of absolute escape fraction, which we define as follows:

$$f_{\rm esc,abs} \equiv \frac{L_{\rm out}^{\rm UV}}{L_{\rm int}^{\rm UV}}, \quad (3)$$

where $L_{\rm int}^{\rm UV}$, $L_{\rm out}^{\rm UV}$ are the intrinsic and emergent UV luminosities measured at the virial radius, respectively. We estimate the escape fractions of ionizing photons ($f_{\rm esc,abs}^{\rm ion}$) and non-ionizing UV continuum ($f_{\rm esc,abs}^{\rm UV}$) for the wavelength range of 1500–2800 Å. We find that $f_{\rm esc,abs}^{\rm UV}$ fluctuates in the range of $\sim$0.2–0.8 at $z \lesssim 10$, but with $f_{\rm esc,abs}^{\rm UV} \gtrsim 0.8$ at $z > 10$. As the gas density ($n_{\rm H}^{\rm c}$) at the Galactic Centre increases, dusty clouds efficiently absorb UV photons, resulting in lower escape fraction. The time-averaged value is $\langle f_{\rm esc,abs}^{\rm UV} \rangle \sim 0.3$ at $z =$ 6–10. Also, $f_{\rm esc,abs}^{\rm ion}$ rapidly changes in the range of $\sim$0.01–0.2, with a time-averaged value of $\langle f_{\rm esc,abs}^{\rm ion} \rangle \sim 0.06$ at $z =$ 6–10. Note that the escape fraction can depend on the numerical resolution, because high-resolution simulations resolve high-density clumps that efficiently absorb ionizing photons (e.g. Yajima, Choi &

Nagamine 2011; Paardekooper, Khochfar & Dalla Vecchia 2013). Ma et al. (2015) suggested that the escape fraction of ionizing photons could be overestimated if the threshold density for star formation was $n_{\rm th} < 1\,{\rm cm}^{-3}$. Our threshold density ($n_{\rm th} = 10\,{\rm cm}^{-3}$) satisfies this condition.

Observationally it is difficult to measure the absolute escape fraction directly, so instead the observers have defined the 'relative' escape fraction which is easier to measure (e.g. Steidel, Pettini & Adelberger 2001; Siana et al. 2007; Vasei et al. 2016):

$$f_{\rm esc,rel} \equiv \frac{f^{\rm ion}_{\rm esc,abs}}{f^{\rm UV}_{\rm esc,abs}} = \frac{(F_{\rm UV}/F_{\rm ion})_{\rm int}}{(F_{\rm UV}/F_{\rm ion})_{\rm obs}} {\rm e}^{\tau_{\rm IGM,ion}}, \quad (4)$$

where $F_{\rm UV}/F_{\rm ion}$ is the ratio of flux densities at non-ionizing UV continuum and ionizing photons. Observational studies have measured this ratio and estimated the relative escape fraction using the estimates from population synthesis models and IGM modelling, e.g. $(f^{\rm ion}_{\rm esc,abs}/f^{\rm UV}_{\rm esc,abs}) \simeq 0.7$ and $\exp(-\tau_{\rm IGM,\,ion}) \simeq 0.4$ (Siana et al. 2007; Vasei et al. 2016). At $z < 2$, only several Lyman-continuum emitters have been observed (Leitet et al. 2011, 2013; Borthakur et al. 2014; Izotov et al. 2016), typically with very low values of $f_{\rm esc,rel} \lesssim 0.1$. At $2 < z < 4$, only a few robust detections have been made by Vanzella et al. (2012, 2015, 2016), Mostardi et al. (2015), and de Barros et al. (2016) using high-resolution HST images. In addition, Micheva et al. (2017) observed 25 candidates of Lyman-continuum emitters at $z = 3.1$ using a narrow-band filter designed to detect ionizing photons at ∼900 Å in the rest frame (see also Iwata et al. 2009) and showed that $f_{\rm esc,rel}$ increased as the UV flux decreased.

Here we show $f_{\rm esc,rel}$ by measuring the ratio $f^{\rm ion}_{\rm esc,abs}/f^{\rm UV}_{\rm esc,abs}$ as in the bottom panel of Fig. 2. We find that $f_{\rm esc,rel}$ fluctuates in the range of ∼0.2–0.8 at $z \gtrsim 10$ and becomes roughly constant with ∼0.2 at $z < 10$. The transition of $f_{\rm esc,rel}$ from higher to lower values as galaxies become brighter is similar to the trend observed in Micheva et al. (2017). In our simulations, ionizing photons can easily escape from galaxies at $z \gtrsim 10$ because most gas can be ejected due to the feedback. However, as the halo mass increases, neutral hydrogen in high-density gas clouds covers star-forming regions and prevents the escape of ionizing photons (see also, Yajima et al. 2011, 2014a). The absorption by neutral hydrogen reduces $f^{\rm ion}_{\rm esc,abs}$ more substantially than $f^{\rm UV}_{\rm esc,abs}$, because only the dust absorption is relevant for $f^{\rm UV}_{\rm esc,abs}$.

In addition, note that $f_{\rm esc,rel}$ is greater than $f^{\rm ion}_{\rm esc,abs}$ at $z \lesssim 10$. This is because $f_{\rm esc,rel}$ does not take into account the dust extinction. As shown in the third panel of Fig. 2, more than half of UV continuum photons are absorbed by dust at $z \sim 6$–10. Therefore we suggest that the dust correction (conversion from $f_{\rm esc,rel}$ to $f^{\rm ion}_{\rm esc,abs}$) is required even for massive galaxies at high redshifts.

The fluctuation of escape fraction in high-z dwarf galaxies ($M_{\rm h} \sim 10^8$–$10^{10.5}$ M$_\odot$) was discussed in previous works (Kimm & Cen 2014; Ma et al. 2015, 2016; Paardekooper et al. 2015; Trebitsch et al. 2017), although they focused on ionizing photons alone. We find that escape fraction becomes very small when the galaxy becomes massive ($M_{\rm h} \sim 10^{10}$–10^{11} M$_\odot$), since most UV photons are absorbed by the central dense gas and dust.

To investigate the cause of fluctuating UV escape fraction, we plot the density distribution of dust and UV optical depths at $z = 8.5$ and 9.0 in Fig. 3. We see that $f^{\rm UV}_{\rm esc}$ is high (0.56) at $z = 8.5$ and becomes low (0.12) at $z = 9.0$. The horizontal axis is the distance from the peak position of local SFR, normalized by the virial radius. The dust density profile is obtained by taking the mean values in each spherical shell. As shown in the figure, the dust is concentrated in the star-forming region at $z = 9.0$, which makes it optically thick.

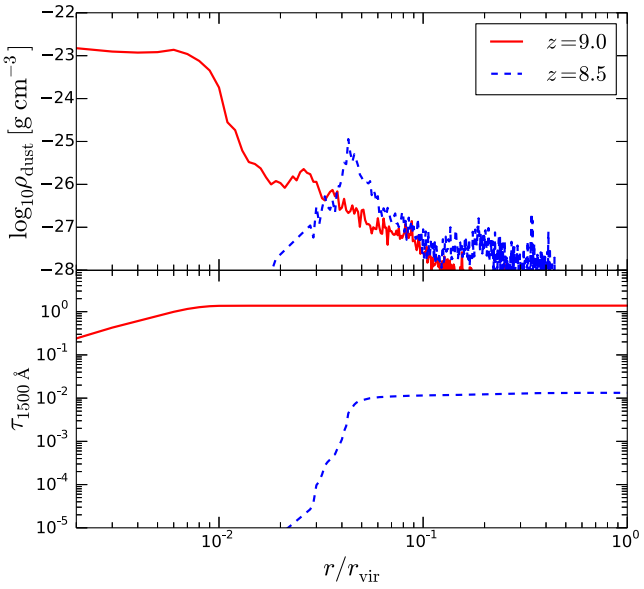

Figure 3. *Top panel*: Radial density profile of dust in Halo-11, measured from the peak position of local SFR. The dust density is computed by taking the mean value in each spherical shell with a width of 16 pc. *Bottom panel*: Optical depth for UV radiation (1500 Å). Red solid and blue dashed lines represent the snapshots when the UV escape fraction is low ($z = 9.0$) and high ($z = 8.5$), respectively.

At $z = 8.5$, dust and gas are ejected due to SN feedback, and the star-forming region becomes optically thin. Thus, we conclude that the time variation of $f^{\rm UV}_{\rm esc}$ is due to the cycle of gas accretion and galactic outflow.

In addition, we consider the time-scale of the transitions based on a simple spherical shell model. At $z < 10$, the total SNe energy released from a single starburst is $\sim 10^{55}(\frac{\rm SFR}{0.1\ {\rm M}_\odot\ {\rm yr}^{-1}})(\frac{t_{\rm life}}{10\ {\rm Myr}})$ erg, where $t_{\rm life}$ is the lifetime of massive stars and we consider the energy of each SN as 10^{51} erg. It easily exceeds the gravitational binding energy of a star-forming gas cloud $E_{\rm b,g} \sim GM^2_{\rm Jeans}/2L_{\rm Jeans} \sim 10^{53}$ erg, as described in Y17 considering the Jeans instability. On the other hand, it is difficult to exceed the binding energy of the host halo, $E_{\rm b,h} \sim 10^{56}(\frac{M_{\rm h}}{10^{10}\ {\rm M}_\odot})^{5/3}(\frac{1+z}{10})(\frac{\Omega_{\rm b}/\Omega_{\rm m}}{0.16})$ erg. Thus, SNe can eject the gas from the central region but not from the halo. Therefore, the outflowing gas shell will stall at a specific radius and fall back to the centre within a free-fall time. The free-fall time for a shell to fall from the virial radius to the centre is $t_{\rm ff} \sim (2r^3_{\rm vir}/GM_{\rm h})^{1/2} \sim 100(\frac{1+z}{10})^{-3/2}$ Myr. This is consistent with our simulation result because the fluctuations occur a few times within 450 Myr ($z = 6$–10).

3.3 Sub-millimeter flux and dependence of halo mass

As $f^{\rm UV}_{\rm esc}$ rapidly changes, galaxies are expected to flicker in both UV and sub-mm wavelengths on short time-scales. Here we investigate the time evolution of sub-mm flux. Since dust extinction is likely to depend on the halo mass (e.g. Yajima et al. 2011, 2014a), we compare the sub-mm fluxes of different haloes.

The top panel of Fig. 4 shows the SF histories of different haloes. All haloes show gradual increase in SFR with decreasing redshift, but with intermittent star formation at $z \gtrsim 10$ which was also discussed in Y17. The second panel shows the rapid fluctuation of $f^{\rm UV}_{\rm esc}$ at $z \gtrsim 10$ together with star formation. As the dust mass increases with galaxy growth, the massive galaxies have lower $f^{\rm UV}_{\rm esc}$

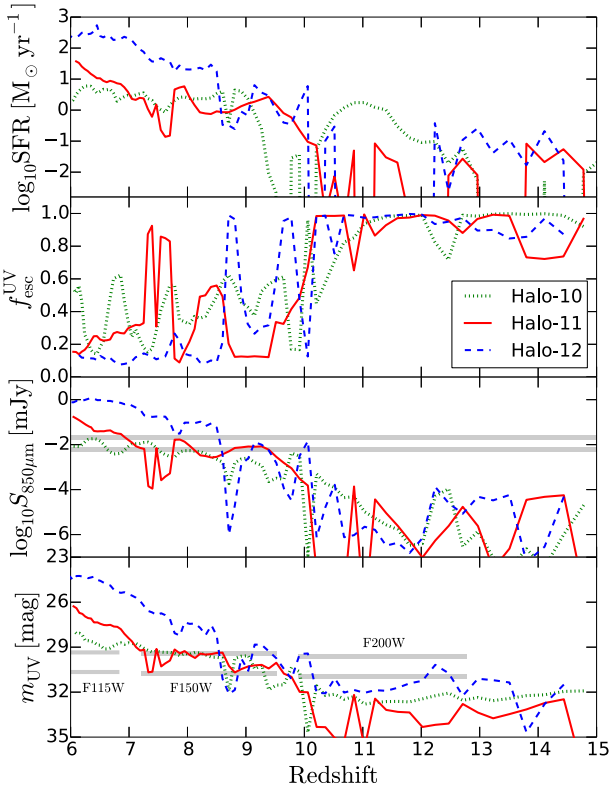

Figure 4. Redshift evolution of SFR (top panel), UV escape fraction (second panel), sub-mm flux (third panel), and emergent UV flux (bottom panel) are shown for Halo-10 (green dotted), Halo-11 (red solid), and Halo-12 (blue dashed). The grey horizontal lines in the third and fourth panels show 3σ (lower line) and 10σ (higher line) detection thresholds for ALMA (full operation) and JWST with 10 h time integration, which we obtained from the online calculators of each observatory.

at $z < 10$: $f_{\rm esc}^{\rm UV} = 0.1$–$0.2$ for Halo-11 (Halo-12) at $z \lesssim 7.5\,(8.5)$, while $f_{\rm esc}^{\rm UV}$ of Halo-10 fluctuates in the range of ∼0.2–0.6 even at $z \sim 6$. In the case of Halo-12, the baryon mass within 200 pc from the Galactic Centre becomes $\sim 10^{10}$ M$_\odot$ at $z \sim 8.5$, and the gravitational binding energy exceeds the thermal energy released by SNe in an intense star formation with SFR $\gtrsim 10$ M$_\odot$ yr^{-1}. Therefore the gas is able to stay around star-forming regions and obscure UV light. These variations of $f_{\rm esc}^{\rm UV}$ for different halo masses are closely linked to the UV luminosity functions. For example, if the UV magnitude of $m_{\rm UV} \sim 30$ fluctuates by a factor of 2 at $z \sim$ 7–8, it can make the luminosity function flatter at the faint end. In our future work, we will investigate the impact of fluctuating escape fraction on the luminosity function using large-scale cosmological simulations.

The third panel of Fig. 4 shows the redshift evolution of sub-mm flux at 850 μm in the observed frame. In all cases, the flux fluctuates by more than an order of magnitude at $z \lesssim 10$ because of the starbursts and low UV escape fractions. When the dusty gas is concentrated at the Galactic Centre, it causes a starburst and obscures the UV light from young stars, resulting in high sub-mm fluxes. The sub-mm flux of Halo-11 (Halo-12) reaches $S_{850\mu{\rm m}}^{\rm obs.} \sim$ 0.1 mJy (1 mJy) at $z \sim$ 6–7, which can be observed by ALMA with $\sim$ 3 h integration time. As a reference, we compare our models with the sensitivity of ALMA 10 h observation as shown in the figure. The Halo-11 is detectable at $z \lesssim 7.3$ or $z \sim 8.0$, 9.0 with 3σ significance. We can compare Halo-11 and Halo-12 with one of the high-z galaxies observed by ALMA, A1689-zD1 at $z \approx 7.5$ (Watson et al. 2015). The sub-mm flux of the galaxy was 0.61 ± 0.12 mJy, and the estimated SFR and dust mass were ~ 12 M$_\odot$ yr^{-1} and $\sim 4 \times 10^7$ M$_\odot$. The A1689-zD1 is a sub-L_* galaxy, thus it was considered as one of the 'normal' galaxies which are the dominant population at that epoch. The dust masses of Halo-11 and Halo-12 at $z = 7.5$ are $\sim 5 \times 10^6$ and $\sim 8 \times 10^7$ M$_\odot$, respectively; thus A1689-zD1 has intermediate parameters of Halo-11 and Halo-12.

In addition to A1689-zD1, the LBGs with sub-mm fluxes of ∼ 0.1 mJy have been detected by recent ALMA observations (Bowler et al. 2018; Hashimoto et al. 2019; Tamura et al. 2019). Halo-11 successfully reproduces the observed sub-mm and UV fluxes of LBGs. However, note that the observations which detect dust continuum emission at only one wavelength has to assume the dust temperature to estimate the SFR or dust mass. If this assumption is not valid, then the estimated physical values could be incorrect. In Section 3.5, we discuss the typical dust temperature in the first galaxies.

The bottom panel of Fig. 4 shows the evolution of apparent UV (1500 Å) magnitude. As a reference, we also show the sensitivity of JWST in the figure. This comparison suggests that the detection of Halo-10 and Halo-11 at $z > 10$ is very difficult, whereas the Ly α flux from the first galaxies can be detected even at $z \gtrsim 10$ (Yajima et al. 2015a). Yajima, Sugimura & Hasegawa (2018) showed that the massive galaxies tend to have higher SFR, and the strong ionizing flux forms huge H II bubbles ($\gtrsim$100 kpc) which increases the IGM transmission of Ly α photons.

3.4 Duty cycle and observability

As we discussed in Section 3.3, the sub-mm brightness of the first galaxies oscillates on a short time-scale. Hereafter, we call this phenomena '*duty cycle*' ($f_{\rm duty}$), and attempt to estimate its value. The duration of the bright phases is directly related to the detection probability of galaxies with a specific mass. Jaacks, Nagamine & Choi (2012b) studied the SF histories of galaxies at $z > 6$ using cosmological hydrodynamic simulations, and estimated the duty cycle defined as the ratio of the number of galaxies which is brighter than the detection limit of the HST to the tota l number.

In this work, we resolve the spatial distribution of dust in detail by using the zoom-in initial conditions and calculating the dust attenuation. Here we estimate $f_{\rm duty}$ based on the detectability of sub-mm fluxes of galaxies by ALMA, and define it as the ratio of number of galaxies brighter than the detection limit ($S_{\rm th}$) at 850 μm to the total number:

$$f_{\rm duty} \equiv \frac{N(S > S_{\rm th})}{N_{\rm tot}}. \quad (5)$$

To increase the number of galaxies, we calculate the radiative properties of all satellite galaxies in the zoom-in regions of fiducial runs (Halo-11 and Halo-12), and include them in our sample. The mass limits of the satellite galaxy selection are $M_{\rm h} > 10^8$ M$_\odot$ for Halo-11 and $M_{\rm h} > 10^9$ M$_\odot$ for Halo-12, respectively. The numbers of galaxies at each snapshot are 613, 593, 564, and 351 at $z \approx 6$, 7, 8, and 10, respectively.

Fig. 5 shows the distribution of halo masses and sub-mm fluxes of our samples at $z \sim$ 10, 8, 7, and 6. With decreasing redshift, one can see that the massive end of the distribution gradually shifts to the right hand side as the haloes grow in their masses. The sharp cut-off at the low-mass end of the distribution of yellow

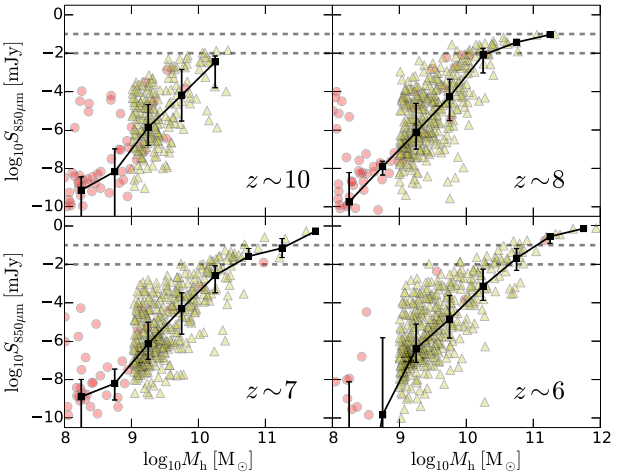

Figure 5. Sub-mm fluxes of all main and satellite galaxies in Halo-11 (red circles) and Halo-12 (yellow triangles) at $z \sim 10$, 8, 7, and 6. Black squares are the median values in each halo mass bin with the width of $\Delta \log_{10}(M_{\rm h}/{\rm M}_\odot) = 0.5$, and the error bars show the quartiles. Dashed lines represent the detection thresholds of $S_{\rm th} = 0.1$ and 0.01 mJy at 850 μm (see Fig. 6).

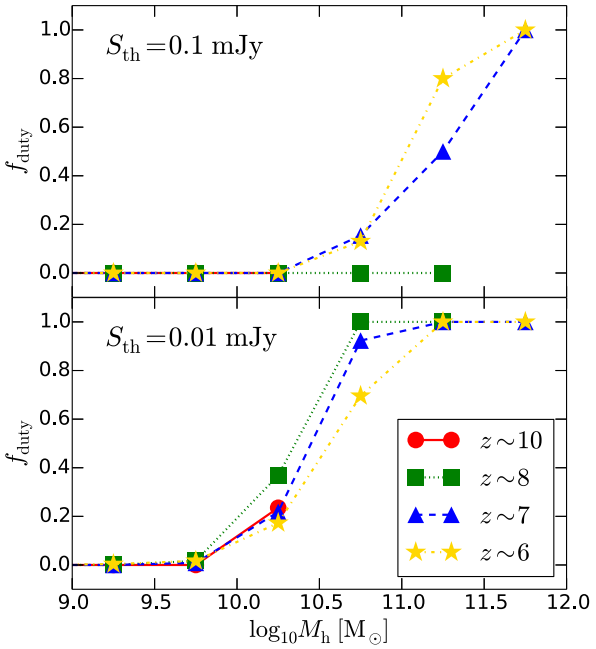

Figure 6. Duty cycle ($f_{\rm duty}$), which is defined as the number fraction of observable galaxies to the total sample in each halo mass bin, is plotted against the halo mass. The top panel shows $f_{\rm duty}$ for the detection threshold of $S_{\rm th} = 0.1$ mJy at 850 μm. This corresponds to 10σ detection by the ALMA observation with 20 min integration with full operation. The bottom panel represents the case of $S_{\rm th} = 0.01$ mJy which corresponds to 10σ detection with 40 h integration.

triangles are due to the halo mass resolution of Halo-12, which corresponds to roughly 10^3 dark matter particles. Halo-11 has higher resolution than Halo-11, and haloes with $M_{\rm h} \gtrsim 10^8\,h^{-1}\,{\rm M}_\odot$ are resolved reasonably well. The sub-mm flux increases steeply with the halo mass because massive galaxies have higher SFRs and lower $f_{\rm esc}$ (see Section 3.3). Star formation of satellite galaxies also occurs intermittently, resulting in the large dispersion of the sub-mm fluxes.

Fig. 6 shows $f_{\rm duty}$ as a function of halo mass. We separate the galaxies into halo mass bins with the bin size of $\Delta \log_{10}(M_{\rm h}/{\rm M}_\odot) = 0.5$ and derive $f_{\rm duty}$ for each bin. Upper and lower panels present $f_{\rm duty}$ for the detection thresholds of $S_{\rm th} = 0.1$ and 0.01 mJy, which corresponds to 10σ detection with 40 min and 60 h observations by ALMA Band-7 full operation, respectively. In the case of $S_{\rm th} = 0.1$ mJy, $f_{\rm duty}$ exceeds 0.5 only for massive haloes with $\log_{10}(M_{\rm h}/{\rm M}_\odot) \geq 11$ at $z \leq 7$, and it changes with redshift only at the massive end. Note that, however, the sample at $M_{\rm h} > 10^{11}$ M$_\odot$ is small ($N \lesssim 10$). Therefore the estimation of $f_{\rm duty}$ at the massive end is likely to contain large uncertainties. In the case of $S_{\rm th} = 0.01$ mJy, $f_{\rm duty}$ steeply increases at lower halo mass and becomes 0.5 at $\log_{10}(M_{\rm h}/{\rm M}_\odot) \approx 10.5$. Therefore deep observations that can observe down to 0.01 mJy will be able to detect the sub-mm fluxes from low-mass galaxies.

By integrating the Sheth & Tormen (2002) halo mass function multiplied by $f_{\rm duty}$, we can roughly estimate the number density of observable sub-mm sources above a certain threshold flux density $S_{\rm th}$, as shown in Fig. 7. In the case of $S_{\rm th} = 0.01$ mJy, the number density increases as redshift decreases, and it becomes 5.4×10^{-3} cMpc^{-3} at $z \sim 6$, which is close to that of LBGs at the same redshift ($\sim 10^{-2}$ cMpc^{-3}; Ouchi et al. 2010; Bouwens et al. 2015). Therefore, we suggest that deep sub-mm observations can detect even typical LBGs. On the other hand, observations with $S_{\rm th} = 0.1$ mJy would not be able to detect typical LBGs. We note that Nagamine, Wolfe & Hernquist (2006) reached similar conclusions based on the results of cosmological hydrodynamic simulations.

As a comparison, we also show the results of the cases with a lower star formation efficiency parameter (Halo-11-lowSF and

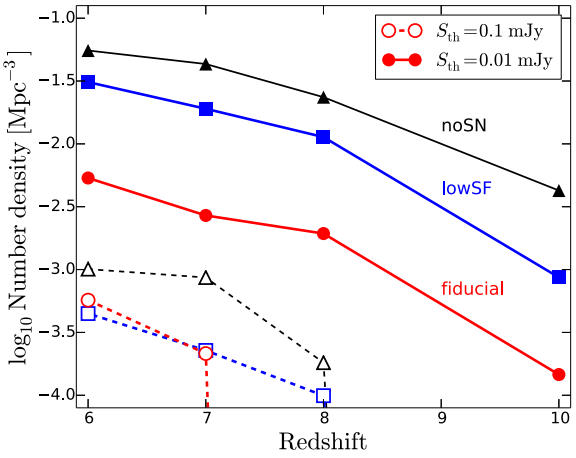

Figure 7. Number density of observable sub-mm sources in units of comoving Mpc^{-3}, which is estimated by integrating the Sheth & Tormen (2002) halo mass function multiplied by the duty cycle. The solid and dashed lines represent the predicted number densities for the detection thresholds of $S_{\rm th} = 0.01$ and 0.1 mJy at 850 μm, respectively. Different colours represent different models: fiducial runs (Halo-11 and Halo-12; red circles), Halo-11-noSN and Halo-12-noSN (black triangles), and Halo-11-lowSF and Halo-12-lowSF (blue squares).

Halo-12-lowSF) and without SN feedback (Halo-11-noSN and Halo-12-noSN). In the no-SN runs, the SFR is high and continuous, and the dusty gas covers the star-forming regions, resulting in a lower escape fraction. Therefore, $f_{\rm duty}$ is higher than in other runs. Similarly, the star formation occurs continuously in Halo-11-lowSF and Halo-12-lowSF runs (see also Yajima et al. 2017a), although

the SN feedback moderately suppresses the SFR. In these runs, the star formation mainly proceeds in high-density gas clouds at Galactic Centres. Due to efficient cooling loss of thermal energy deposited by SN feedback, strong galactic wind is not launched from high-density gas clouds. Therefore, the time-averaged SFR of intermediate-mass haloes is higher than that in the fiducial runs, and $f_{\rm duty}$ for $S_{\rm th} = 0.01$ mJy becomes higher. However, as the halo mass increases, the deep gravitational potential well can keep the gas gravitationally bound under the impact of SN feedback even in the fiducial runs, which allows massive galaxies to form stars continuously. As a result, the SFR and $f_{\rm esc}$ of massive galaxies in the fiducial runs become similar to the case with a lower star formation efficiency parameter. Thus, there is no significant difference in $f_{\rm duty}$ for the above models. We suggest that a future deep sub-millimeter galaxy survey with a detection threshold of $S_{\rm th} = 0.01$ mJy may be able to constrain the models of star formation and stellar feedback by comparing observations with theoretical models.

The impact of sub-grid models on star formation and feedback has also been studied by comparing with the observations of local galaxies (e.g. Okamoto, Shimizu & Yoshida 2014; Schaye et al. 2015; Pillepich et al. 2018). They showed that the SN feedback model should be tuned to reproduce the observations, e.g. the stellar mass function (Crain et al. 2015). On the other hand, the star formation model may not change the star formation history significantly. Schaye et al. (2010) showed that the cosmic SFR density was insensitive to the star formation parameter, i.e. 'A' in equation (1) of this paper. As in Fig. 14, our simulations also showed that the difference of SFR between Halo-11 and Halo-11-lowSF becomes small at $z \lesssim 8$. Note that, however, the number density of faint sub-mm sources of low-SF runs is higher than that of fiducial runs (Halo-11 and Halo-12) by a factor ∼2–3 even at $z \lesssim 8$ due to different distribution of dusty gas. Therefore, we suggest that the comparisons between theoretical models and the observations of sub-mm sources can be a complementary tool to study the validity of star formation models.

In addition, Cullen et al. (2019) studied the stellar mass–metallicity relation (MZR) at high redshift, and they found that the FiBY simulations reproduced the slope of observed MZR well, however there was a difference in the normalization by a factor of a few. Comparing with other simulation projects, they argued that the SN feedback model was critically important for the MZR because it controlled the transport rates of metal and dust into the CGM and IGM. We show that the SN feedback model also affects the dust obscuration, which could result in strong variations in the observed number density of ALMA sources.

In addition, Fig. 8 presents the relation between SFR and IR luminosity at $z = 7$. For the star-forming galaxies, the IR luminosity increases with SFR because young stars dominantly generate the UV photons which are absorbed and reprocessed by dust. The power-law fit of the relation follows as

$$L_{\rm IR} \approx 3.2 \times 10^9\,{\rm L}_\odot \left(\frac{\rm SFR}{\rm M_\odot\,yr^{-1}}\right)^{1.21}, \quad (6)$$

where we used the galaxy sample with $-4 < \log_{10}{\rm SFR\,[M_\odot\,yr^{-1}]} < 3$ for the fitting. If the dust completely absorbs UV photons, the power index must be unity because UV luminosity relates to SFR linearly. In our simulation, however, the low-mass galaxies have low SFR and high escape fraction of UV photons, resulting in low IR luminosity. We find that this effect makes the relation steeper. The relation can reproduce the observed

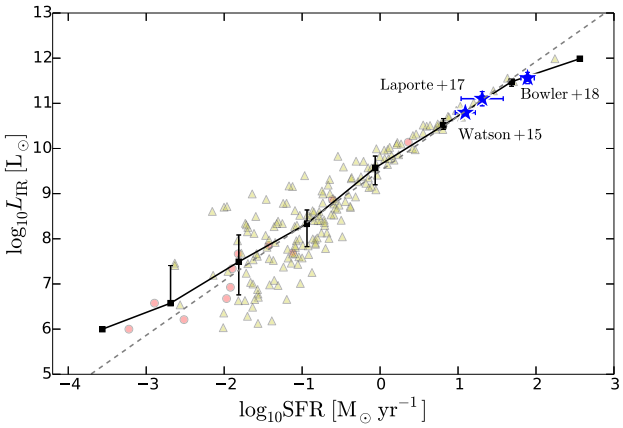

Figure 8. Relation between SFR and IR luminosity at $z = 7$. Meaning of the symbols is the same as in Fig. 5. The dashed line shows the power-law fit (equation 6) for star-forming galaxies. The blue stars represent observed LBGs at $z \sim 7$–8 (Watson et al. 2015; Laporte et al. 2017; Bowler et al. 2018).

LBGs at $z \sim 7$–8 (Watson et al. 2015; Laporte et al. 2017; Bowler et al. 2018) remarkably well, whose SFRs were measured from the UV and IR luminosity. Meanwhile, non-star-forming galaxies also have large dispersion of IR luminosity due to the dust absorption of UV photons emitted by residual young stars.

Here we overview how dust attenuation affects observation. The top panel of Fig. 9 presents the relation between the intrinsic UV absolute magnitude and the emergent one, i.e. before and after the dust absorption in each galaxy. For the faint galaxies dimmer than $M_{\rm int}^{\rm UV} \sim -17$, most of the UV photons escape from the haloes, resulting in a tight linear relation between the emergent luminosities and the intrinsic ones. For the galaxies brighter than $M_{\rm int}^{\rm UV} \sim -19$, the dust attenuation significantly decreases the UV luminosity (escape fraction ∼0.1, see also Ma et al. 2018b).

The bottom panel of Fig. 9 shows the relation between the intrinsic apparent magnitude and the sub-mm flux in the observed frame. The observed sub-mm flux decreases as $m_{\rm int}^{\rm UV}$ becomes fainter, and they reach the detection limit of ALMA ($\gtrsim$0.01 mJy) at $m_{\rm int}^{\rm UV} \sim 27$. For the galaxies fainter than $m_{\rm int}^{\rm UV} \sim 29$ mag, the escape fraction rapidly changes between 0.2–0.8 due to intermittent star formation, resulting in dispersion of $\Delta m \sim 1.5$ for the observed magnitude.

3.5 Dust temperature

The dust temperature is an important factor in estimating the bolometric infrared luminosity, but it has not been estimated well for the first galaxies so far due to limited observational data. In infrared observations of local galaxies, the flux at some different frequencies can be detected, and the dust temperature is determined from the peak wavelength of modified blackbody spectrum (e.g. Hwang et al. 2010). On the other hand, most of the ALMA observations of high-z galaxies have obtained the flux only at one wavelength. Therefore the dust mass or SFR have been estimated based on the assumed dust temperature (e.g. ∼40 K, Watson et al. 2015). Here we investigate the typical dust temperature of first galaxies.

To describe the spatial distribution of dust temperature, we present the 2D map in the lower left panel of Fig. 1, which displays the mass-weighted mean temperature along the line of sight. In the

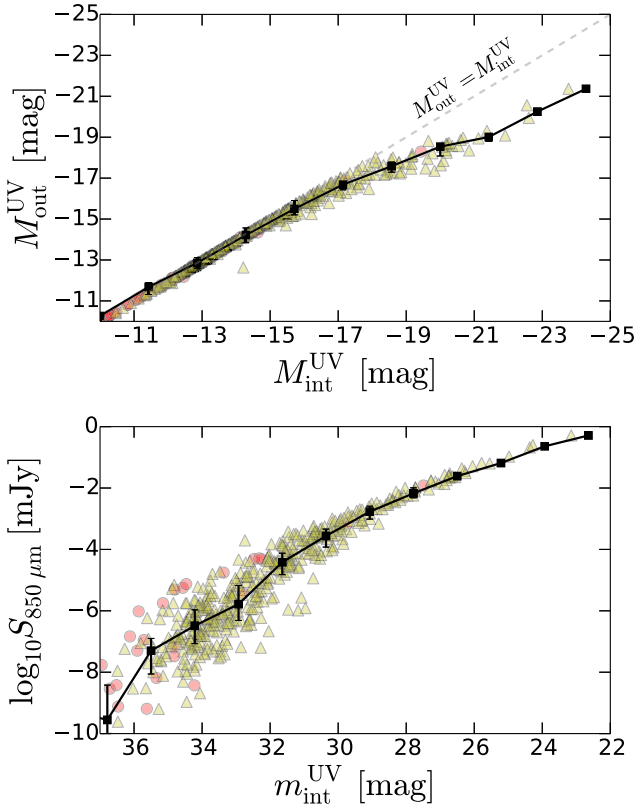

Figure 9. Upper panel: Relation between intrinsic rest-frame UV absolute magnitudes and emergent ones of the main halo and satellites in Halo-11 (red circle) and Halo-12 (yellow triangle) at $z \sim 7$. The black squares and error bars show the medians and quartiles within each bin, respectively. The dashed line describes the case in which all of UV photons can escape from the halo. One can see that the dust attenuation strongly affects the UV magnitude by $\Delta M \sim 2$ mag for the bright galaxies. Lower panel: Relation between the intrinsic UV apparent magnitude and observed sub-mm flux of simulated galaxies.

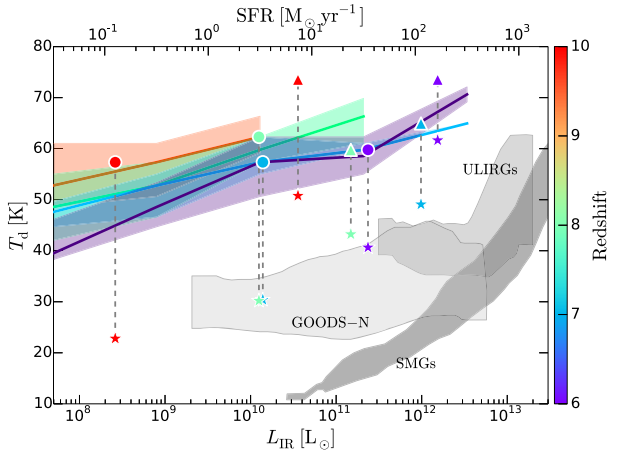

Figure 10. Relation between dust temperature and bolometric infrared luminosity. The upper horizontal axis indicates SFR derived from equation (6). Filled circles show the dust temperature measured from the peak wavelength of modified SEDs. Different colours mean different redshifts: $z = 6$ (purple), $z = 7$ (cyan), $z = 8$ (green), and $z = 10$ (red). Colour-shaded regions indicate the ranges of dust temperatures of all satellite galaxies. Filled stars show the mean dust temperature weighted by dust mass of main haloes. Grey shaded regions represent the range of dust temperatures of observed sub-mm galaxies (SMGs) at $z \sim$ 1–3 (Chapman et al. 2005; Kovács et al. 2006), ultraluminous infrared galaxies (ULIRGs) at $z < 1$ (Yang et al. 2007; Younger et al. 2009), and typical star-forming galaxies at $z \sim 0.1$–2.8 (Hwang et al. 2010).

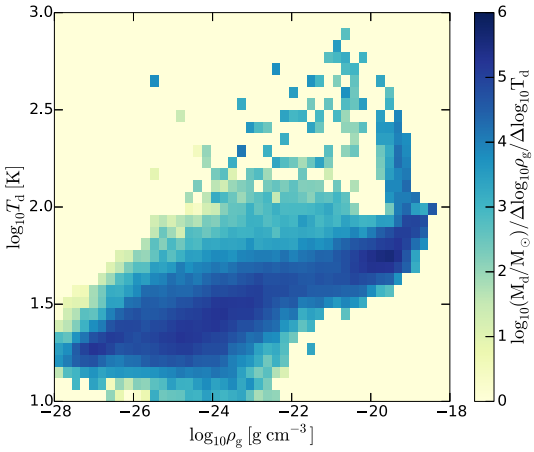

Figure 11. Distribution of dust mass as functions of gas density and dust temperature in Halo-11 at $z \sim 6$. The cool dust ($\lesssim$40 K, $\sim 1.2 \times 10^7$ $M_\odot$) exists in the outer low-density regions, and the hot dust ($\gtrsim$40 K, $\sim 5 \times 10^6$ $M_\odot$) heated by stellar UV radiation exists in the central high-density regions.

outer parts of the galaxy, cool dust ($T_{\rm d} \sim 30$ K) dominates, while at the central star-forming region dust temperature is high ($T_{\rm d} \sim 60$ K) due to strong UV irradiation.

Fig. 10 shows the relation between dust temperature and total IR (3–1000 μm) luminosity for the main and satellite galaxies in Halo-11 and Halo-12 at $z =$ 6–10. We estimate the dust temperature from the peak wavelength of SEDs with modified blackbody spectrum considering the absorption efficiency of our dust model. The temperature increases from ∼40 to ∼70 K as the IR luminosity increases from $\sim 10^8$ to $\sim 10^{12}$ $L_\odot$. Since high IR luminosity corresponds to intense star formation (Fig. 8), the emitted UV photons heat dust efficiently. For bright galaxies ($L_{\rm IR} > 10^{10}$ $L_\odot$) the temperatures are higher than that of nearby star-forming galaxies, local ultraluminous infrared galaxies (ULIRGs), and low-z SMGs (shaded areas, Hwang et al. 2010) by about 10–20 K. The compactness of high-z galaxies induces formation of dense star-forming gas clumps and radiative heating of dust (see also Behrens et al. 2018). In addition, Fig. 10 also displays mass-weighted mean dust temperatures by the star symbols, which are lower than $T_{\rm peak}$ by ∼20–40 K. This indicates that some fraction of dust is in cold state with $T \lesssim 30$ K.

Fig. 11 shows the distribution of dust mass as functions of gas density and dust temperature. We can see the evolution of dust temperature on the figure. In the outer low-density regions, a large amount of dust have a temperature similar to the CMB temperature (∼30 K). As dust is accreted on to the Galactic Centre, dust temperature increases to ∼100 K due to strong irradiation of stellar UV photons. Observational studies of high-z galaxies using flux of 850 μm estimated the amount of central hot dust (see Fig. 1), however, our simulation suggests that there is comparable amount of dust in the outer part of the halo. The longer wavelength observation would be studying the distribution of cooler dust in the outer parts of high-z galaxies.

As redshift increases, galaxies become more compact (∼10 per cent of virial radius, see Section 3.6). Therefore we expect that dust also distribute compactly, resulting in efficient heating of dust by intense stellar UV flux. Here we estimate the typical distance of dusty clouds from star-forming regions under the assumption of radiative equilibrium as

$$R = \left(\frac{L_{\rm UV}}{16\pi^2 \int Q_\nu B_\nu(T_{\rm d}) {\rm d}\nu} \right)^{1/2}, \quad (7)$$

where Q_ν is the absorption efficiency to the geometrical cross-section of dust. Here we use Q_ν estimated in Laor & Draine (1993). In the case of our simulated dust temperature $T_{\rm d} \sim 50$–70 K and $L_{\rm UV} = L_{\rm IR} = 10^{11}\ L_\odot$, the typical distance is 1–3 kpc, which is similar to the disc sizes of high-z galaxies. Note that, however, the dust temperature depends on not only the compactness, but also the size of dust grains. Nozawa et al. (2007) suggested that the dust size ranged $\gtrsim 0.1$ μm because small dust grains with < 0.1 μm could be destroyed due to reverse shocks in SN remnants. If we consider different dust model with larger grain sizes, the dust temperature will decrease (e.g. Yajima et al. 2014b, 2017b).

The relation between $L_{\rm IR}/L_{\rm UV}$ ratio (IRX) and the UV slope $\beta_{\rm UV}$ is often used to predict the dust properties of high-z galaxies (e.g. Meurer, Heckman & Calzetti 1999). Recently, Capak et al. (2015) and Bouwens et al. (2016) investigated the IRX–$\beta_{\rm UV}$ relation of galaxies at $z \sim 6$ with ALMA, and they found that most of the galaxies had lower IRX for a specific $\beta_{\rm UV}$ than that of local star-forming galaxies and the SMC-type galaxies (e.g. Calzetti et al. 2000). Using the local analogues, Faisst et al. (2017) argued that the typical dust temperature of high-z galaxies was higher than the previous estimates of $T_{\rm d} \sim 30$ K (see also, Ouchi et al. 1999). Our simulations support high dust temperature, which owes to the compactness of dusty clouds and strong UV irradiation from nearby star formation activities. Recently, Ma et al. (2019) investigated the IRX–$\beta_{\rm UV}$ relation of high-z galaxies in cosmological simulations. They showed that the IRXs of high-z galaxies were consistent with the LMC dust model, and that the typical peak wavelength of dust thermal emission was shorter than the local or intermediate redshift galaxies, which implied that the starburst efficiently heated the compactly distributed dust (see also, Behrens et al. 2018). This trend is consistent with our simulations. However, we note that Casey et al. (2018) argued that the hot dust is not necessarily needed to explain the observed dust characteristics of high-z galaxies; namely, the tension between IRX$-\beta_{\rm UV}$ relation for high-z galaxies and the local relation can also be eased by a cool dust temperature and a mid-IR power-law component. Future multiband observations of dust continuum flux will be able to validate these theoretical predictions.

3.6 Size evolution

In this subsection we investigate the time evolution of galaxy sizes. In the classical picture, the disc size is proportional to the angular momentum of accreted gas (Mo, Mao & White 1998). However, Genel et al. (2015) showed that the galactic angular momentum was redistributed due to stellar feedback in the Illustris simulation (see also Scannapieco et al. 2008; Zavala, Okamoto & Frenk 2008). They found that the feedback processes change the galactic morphologies and reproduce the observational relation (Fall & Romanowsky 2013) between the specific angular momentum and stellar mass at $z = 0$. Here we discuss how the sizes of clumpy high-z galaxies change with time and affect the detectability of galaxies. Our simulated galaxies have discs at $z \lesssim 10$, and the sizes are affected by SN feedback as described in Y17.

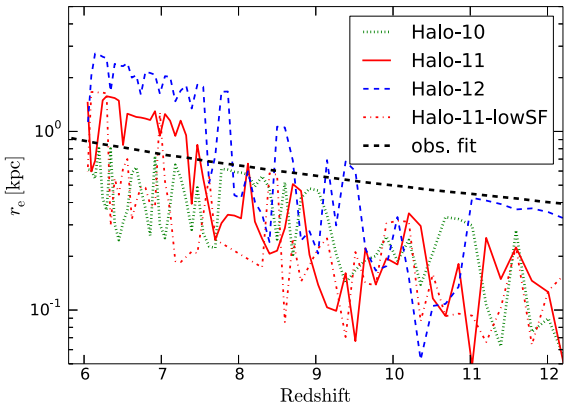

Figure 12. Redshift evolution of the half-light radius of the main galaxy in Halo-10 (green dotted), 11 (red solid), and 12 (blue dashed), derived from the UV surface brightness distribution. Red dot–dashed line shows the half-light radius of Halo-11-lowSF. Black dashed line shows observational fit which use bright galaxies of $-21 \lesssim M_{\rm UV} \lesssim -20.15$ (Kawamata et al. 2018).

Fig. 12 shows the UV half-light radii ($r_{\rm e}$) of Halo-10, Halo-11, and Halo-12 as a function of redshift. Here we define $r_{\rm e}$ (in physical kpc) as the distance from the brightest pixel within which the integrated brightness is half of total luminosity. In the case of merging galaxies, companion galaxies may make $r_{\rm e}$ too large artificially. Therefore we set the upper limit of $r_{\rm e}$ as 10 per cent of virial radius. We observe that $r_{\rm e}$ fluctuates around 0.02–0.1 times the virial radius. When the SFR becomes high, stars and gas are distributed at the Galactic Centre compactly, resulting in smaller $r_{\rm e}$. Meanwhile, $r_{\rm e}$ reaches the upper limit ($0.1 r_{\rm vir}$) when the main galaxies interact with satellite galaxies. In addition, $r_{\rm e}$ gradually increases with the virial radius ($\propto M_{\rm h}^{1/3}(1+z)^{-1}$) as redshift decreases. Finally, the galactic size becomes ∼1 kpc at $z \sim 6$, and more massive galaxy has a larger size.

Understanding the size distribution of high-z galaxies is crucially important for the incompleteness correction in deriving a luminosity function (LF). Extended galaxies are more unlikely to be detected for a given magnitude limit, or some fraction of their flux is lost due to the limited sensitivity. This affects the estimation of faint-end slope of UV LFs (Grazian et al. 2011).

Fig. 13 shows the size–luminosity (RL) relation of all satellite galaxies in the zoom-in regions of Halo-11 and Halo-12 at $z \sim$ 6–10. Kawamata et al. (2018) conducted simultaneous maximum-likelihood estimation of LF and RL relation for galaxies at $z > 6$, and they found that the slope β for the RL relation $r_{\rm e} \propto L^\beta$ is ∼0.4. For the bright galaxies ($M_{\rm UV} < -15$) at $z \sim$ 6–8, our results match the observational data well.

On the other hand, the faint galaxies ($M_{\rm UV} \gtrsim -15$) have a larger dispersion and their sizes are away from the observational fit. This can be related to the intermittent star formation histories of low-mass galaxies. Stellar feedback induces the angular momentum redistribution of gas disc and make the stellar distribution extended (see also, El-Badry et al. 2016). Another reason is the rapid change of local gravitational potential due to feedback. If star clusters are virialized with the local gravitational potential, they can spread out with the gas outflow. In addition, the quenching time of star formation becomes longer as the galaxy mass decreases, resulting in larger size decided by extended residual stars (in contrast, when

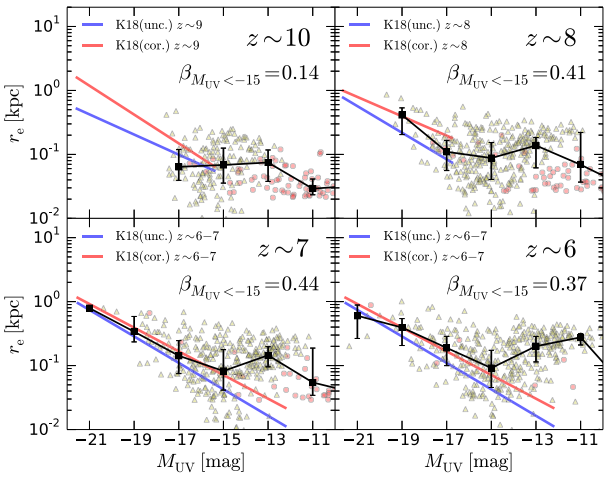

Figure 13. Size–luminosity relation of all galaxies within the zoom-in region of Halo-11 (red circles) and Halo-12 (yellow triangles) at $z \sim 6$, 7, 8, and 10. Black squares and error bars represent the medians and the quantiles within each magnitude bin of $\Delta M_{UV} = 2.0$ mag. We compute the slope β for the relation $r_e \propto L^{\beta}$ for the simulated galaxies with brighter than $M_{UV} = -15$. The red and blue lines show the fit to the observational result by Kawamata et al. (2018), with and without the incompleteness correction, respectively.

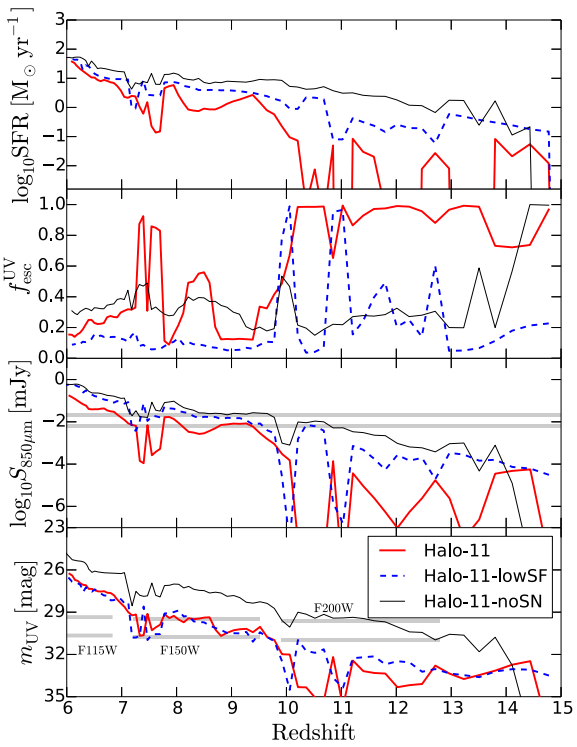

Figure 14. Same as Fig. 4 but for the cases of Halo-11, Halo-11-lowSF, and Halo-11-noSN.

galaxies have star formation, the star-forming clump is main source of UV light, resulting in smaller r_e). These effects might turn the RL relation up at the faint end ($M_{UV} \gtrsim -13$). Thus, we suggest that some fraction of low-mass galaxies could be lost in observation due to the extended stellar distribution and faint surface brightness. This could change the faint-end slope of observed LFs. Note that Ma et al. (2018a) also showed the large dispersion of galaxy sizes at the faint end. They argued that if the sensitivity for surface brightness was lower than ~ 25.5 mag arcsec^{-2}, the size measurement was biased by bright star-forming clumps, resulting in the underestimation of sizes. To avoid picking up multiple clumps of low-mass galaxies which could boost up the value of r_e, we did not include the galaxies that are larger than 10 per cent of virial radii.

Note that, however, the galactic size or 'compactness' can be affected by star formation model as described in Y17. In addition, Wyithe & Loeb (2011) pointed out that the RL relation is also affected by SN feedback model. We also present the size evolution of Halo-11-lowSF to show the difference from that of Halo-11. The inefficient star formation allows the formation of very dense and compact gas clumps at Galactic Centres, which efficiently traps UV photons. Thus r_e stays at lower value for most of the time. We discuss more details of model dependence in Section 4.

4 DISCUSSION

We have studied the radiative properties of different haloes simulated with the same star formation and feedback models. Here we investigate how the radiative properties change if we decrease the star formation efficiency (Halo-11-lowSF) or turn-off the SN feedback (Halo-11-noSN). Recent observations suggested that the amplitude factor of Kennicutt–Schmidt law was much higher than the local galaxies for merging galaxies (Genzel et al. 2010) or high-redshift galaxies (Tacconi et al. 2013). Therefore Y17 used a high-amplitude factor of $A = 1.5 \times 10^{-3}$ $M_\odot$ yr^{-1} kpc^{-1} which was higher than that of the local galaxies by a factor 10 (see also Khochfar & Silk 2011; Silk 2013). Halo-11-lowSF uses the amplitude factor same as the local galaxies, i.e. $A = 1.5 \times 10^{-4}$ $M_\odot$ yr^{-1} kpc^{-1}.

Fig. 14 shows the star formation histories and radiative properties of Halo-11, Halo-11-lowSF, and Halo-11-noSN. In the case of Halo-11-lowSF, the star formation occurs continuously because the central gas density is very high, which makes the SN feedback inefficient due to the efficient radiative cooling (see the details in Y17). Therefore, the gas clouds are not completely disrupted and the continuous star formation is allowed. The star-forming gas clouds also efficiently absorb stellar UV radiation, resulting in the low escape fraction as shown in the second panel of the figure. In the case of Halo-11-noSN, most of the gas is rapidly converted into stars, resulting in the lower gas density than that of Halo-11-lowSF. Therefore f_{esc}^{UV} of Halo-11-noSN is higher than that of Halo-11-lowSF. Also f_{esc}^{UV} does not change with time significantly due to lack of feedback.

In Halo-11-lowSF and Halo-11-noSN, the SFR is higher than Halo-11, and f_{esc}^{UV} is lower, resulting in higher sub-mm flux than Halo-11. In addition, the difference between Halo-11-lowSF and Halo-11-noSN clearly appears in the UV magnitude due to different escape fraction. Thus we argue that the radiative properties of first galaxies sensitively depend on the star formation and feedback models.

5 SUMMARY

In this paper we have studied the radiative properties of first galaxies at $z = 6$–15 by combining cosmological hydrodynamic simulations and radiative transfer calculations. Using zoom-in initial conditions, we follow the formation and evolution of three haloes: Halo-10 ($M_h = 2.4 \times 10^{10}$ $M_\odot$), Halo-11 ($M_h = 1.6 \times 10^{11}$ $M_\odot$), and

Halo-12 ($M_{\rm h} = 0.7 \times 10^{12}$ M$_\odot$) at $z = 6$. Our major findings are as follows:

(i) In the first galaxies, the SN feedback ejects most gas and dust from galaxies, resulting in the intermittent star formation history. This causes the large fluctuation of escape fraction of UV photons. The escape fraction of Halo-11 changes in the range of ∼0.2–0.8 at $z < 10$. As the halo becomes more massive, the fluctuation is suppressed, and the escape fraction remains low at $\lesssim$0.2. The transition redshifts are ∼8.5 for Halo-12 and ∼7.5 for Halo-11. In the case of Halo-10, the escape fraction keeps fluctuating down to $z = 6$.

(ii) Stellar UV radiation absorbed by dust is reprocessed into IR thermal emission. Therefore, the IR flux from galaxies also change with time as the UV escape fraction fluctuates. This fluctuation of the IR flux affects the detectability in sub-mm observations. Using all satellite galaxies within the zoom-in regions, we calculate the detectability by ALMA telescope. If we set the detection threshold to 0.1 mJy at 850 μm, the detectability are $\gtrsim$0.5 for galaxies with the halo mass of $\gtrsim 10^{11}$ M$_\odot$ at $z \lesssim 7$.

(iii) We calculate the three-dimensional structure of dust temperature, and derive SEDs. By using the peak wavelength of infrared flux, we estimate the typical dust temperature of modelled galaxies. The galaxies with $L_{\rm IR} \lesssim 10^{11}\ L_\odot$ have $T_{\rm d} \sim 60$ K that is higher than that of observed galaxies at $z < 3$ (Hwang et al. 2010). Since it is difficult to measure the dust temperature of observed galaxies at $z \geq 6$, the dust temperature of ~ 40 K is frequently assumed in the observations (e.g. Watson et al. 2015). Our simulation suggests that the dust temperatures for high-z galaxies are somewhat higher than the assumed ones, which will change the estimated dust masses and SFRs.

(iv) The half-light radius ($r_{\rm e}$) at UV wavelength fluctuates in the range of $r_{\rm e}/r_{\rm vir} \sim 0.02$–$0.1$, and it increases with time. At $z \sim 6$–8, $r_{\rm e}$ becomes ~ 1 kpc (physical), and the bright galaxies in our simulations ($M_{\rm UV} < -15$) has the relation $r_{\rm e} \propto L^\beta$, where $\beta \sim 0.4$. These are consistent with the observations of Kawamata et al. (2018). When the surface brightness of galaxies is extended, some parts of UV flux can be lost below observational threshold due to cosmological surface brightness dimming.

(v) We compare our fiducial model (Halo-11) with the different models with a low star formation amplitude factor (Halo-11-lowSF) and without the SN feedback (Halo-11-noSN). In cases of Halo-11-lowSF and Halo-11-noSN, massive dusty gas accumulates at the Galactic Centre due to the weak or no SN feedback. This causes higher SFR and lower UV escape fraction than the fiducial model. Therefore, the IR flux of Halo-11-lowSF and Halo-11-noSN is higher than that of Halo-11. Thus we argue that the star formation and feedback models for the first galaxies could be constrained by future observations.

In this work, we investigated the time evolution of radiative properties of the first galaxies, and suggested that the first galaxies rapidly changed from UV-bright to IR-bright phases due to intermittent star formation and SN feedback. However, the sample of simulated galaxies is not large enough to make a statistical comparison to observations. We will obtain a larger galaxy sample using larger scale and higher resolution cosmological simulations, and present the statistical properties, e.g. the luminosity function and cosmic SFR density, taking the detailed radiative processes into account in our future paper. Furthermore, the radiative properties of galaxies depend on the dust properties, e.g. size distribution and compositions (e.g. Aoyama et al. 2017, 2018, 2019a; Hou et al. 2017, 2019; McKinnon et al. 2018; Aoyama, Hirashita & Nagamine 2019b), therefore we will implement a model of dust destruction and production in cosmological simulations, coupled with radiative transfer calculations.

ACKNOWLEDGEMENTS

We thank the referee for the constructive comments. Numerical computations were carried out on the Cray XC30 and XC50 at the Center for Computational Astrophysics, National Astronomical Observatory of Japan, and the OCTOPUS at the Cybermedia Center, Osaka University. This work is supported in part by the MEXT/JSPS KAKENHI Grant Number JP17H04827 (HY), 18H04570 (HY), and JP17H01111 (KN). YL acknowledges support from National Science Foundation through grants AST-1412719 and MRI-1626251. We are grateful to Dr. Ouchi for helpful comments on the dust temperature. KN thanks to Dr. Kawamata for useful discussions on galaxy size evolution. KN acknowledges the travel support from the Kavli IPMU, World Premier Research Center Initiative (WPI), where part of this work was conducted.

REFERENCES

Andre P., Ward-Thompson D., Motte F., 1996, A&A, 314, 625
Aoyama S., Hou K.-C., Shimizu I., Hirashita H., Todoroki K., Choi J.-H., Nagamine K., 2017, MNRAS, 466, 105
Aoyama S., Hou K.-C., Hirashita H., Nagamine K., Shimizu I., 2018, MNRAS, 478, 4905
Aoyama S., Hirashita H., Lim C.-F., Chang Y.-Y., Wang W.-H., Nagamine K., Hou K.-C., Shimizu I., 2019a, MNRAS, 484, 1852
Aoyama S., Hirashita H., Nagamine K., 2019b, preprint (arXiv:1906.01917)
Arata S., Yajima H., Nagamine K., 2018, MNRAS, 475, 4252
Asano R. S., Takeuchi T. T., Hirashita H., Inoue A. K., 2013, Earth Planets Space, 65, 213
Barrow K. S. S., Wise J. H., Aykutalp A., O'Shea B. W., Norman M. L., Xu H., 2018, MNRAS, 474, 2617
Behrens C., Pallottini A., Ferrara A., Gallerani S., Vallini L., 2018, MNRAS, 477, 552
Borthakur S., Heckman T. M., Leitherer C., Overzier R. A., 2014, Science, 346, 216
Bouwens R. J. et al., 2015, ApJ, 803, 34
Bouwens R. J. et al., 2016, ApJ, 833, 72
Bowler R. A. A., Bourne N., Dunlop J. S., McLure R. M., McLeod D. J., 2018, MNRAS, 481, 1631
Calzetti D., Armus L., Bohlin R. C., Kinney A. L., Koornneef J., Storchi-Bergmann T., 2000, ApJ, 533, 682
Capak P. L. et al., 2015, Nature, 522, 455
Casey C. M., Hodge J., Zavala J. A., Spilker J., da Cunha E., Staguhn J., Finkelstein S. L., Drew P., 2018, ApJ, 862, 78
Chabrier G., 2003, PASP, 115, 763
Chapman S. C., Blain A. W., Smail I., Ivison R. J., 2005, ApJ, 622, 772
Chiaki G., Yoshida N., Kitayama T., 2013, ApJ, 762, 50
Chiaki G., Marassi S., Nozawa T., Yoshida N., Schneider R., Omukai K., Limongi M., Chieffi A., 2015, MNRAS, 446, 2659
Crain R. A. et al., 2015, MNRAS, 450, 1937
Cullen F., McLure R. J., Khochfar S., Dunlop J. S., Dalla Vecchia C., 2017, MNRAS, 470, 3006
Cullen F. et al., 2018, MNRAS, 476, 3218
Cullen F. et al., 2019, MNRAS, 487, 2038
Dalla Vecchia C., Schaye J., 2012, MNRAS, 426, 140
Davis A. J., Khochfar S., Dalla Vecchia C., 2014, MNRAS, 443, 985
Dawson S. et al., 2004, ApJ, 617, 707
de Barros S. et al., 2016, A&A, 585, A51
Draine B. T. et al., 2007, ApJ, 663, 866
El-Badry K., Wetzel A., Geha M., Hopkins P. F., Kereš D., Chan T. K., Faucher-Giguère C.-A., 2016, ApJ, 820, 131

Faisst A. L. et al., 2017, ApJ, 847, 21
Fall S. M., Romanowsky A. J., 2013, ApJ, 769, L26
Field G. B., 1965, ApJ, 142, 531
Finkelstein S. L. et al., 2013, Nature, 502, 524
Finkelstein S. L. et al., 2015, ApJ, 810, 71
Genel S., Fall S. M., Hernquist L., Vogelsberger M., Snyder G. F., Rodriguez-Gomez V., Sijacki D., Springel V., 2015, ApJ, 804, L40
Genzel R. et al., 2010, MNRAS, 407, 2091
Grazian A. et al., 2011, A&A, 532, A33
Greif T. H., Johnson J. L., Klessen R. S., Bromm V., 2008, MNRAS, 387, 1021
Gronwall C. et al., 2007, ApJ, 667, 79
Hashimoto T. et al., 2018, Nature, 557, 392
Hashimoto T. et al., 2019, PASJ, 70, preprint (arXiv:1806.00486)
Hirashita H., Kuo T.-M., 2011, MNRAS, 416, 1340
Hopkins P. F., Kereš D., Oñorbe J., Faucher-Giguère C.-A., Quataert E., Murray N., Bullock J. S., 2014, MNRAS, 445, 581
Hou K.-C., Hirashita H., Nagamine K., Aoyama S., Shimizu I., 2017, MNRAS, 469, 870
Hou K.-C., Aoyama S., Hirashita H., Nagamine K., Shimizu I., 2019, MNRAS, 485, 1727
Hu E. M., Cowie L. L., Capak P., McMahon R. G., Hayashino T., Komiyama Y., 2004, AJ, 127, 563
Hwang H. S. et al., 2010, MNRAS, 409, 75
Inoue T., Omukai K., 2015, ApJ, 805, 73
Inoue A. K. et al., 2016, Science, 352, 1559
Iwata I. et al., 2009, ApJ, 692, 1287
Izotov Y. I., Orlitová I., Schaerer D., Thuan T. X., Verhamme A., Guseva N. G., Worseck G., 2016, Nature, 529, 178
Jaacks J., Choi J.-H., Nagamine K., Thompson R., Varghese S., 2012a, MNRAS, 420, 1606
Jaacks J., Nagamine K., Choi J. H., 2012b, MNRAS, 427, 403
Johnson J. L., Dalla Vecchia C., Khochfar S., 2013, MNRAS, 428, 1857
Kashikawa N. et al., 2006, ApJ, 648, 7
Kawamata R., Ishigaki M., Shimasaku K., Oguri M., Ouchi M., Tanigawa S., 2018, ApJ, 855, 4
Kennicutt R. C., Jr, 1998, ARA&A, 36, 189
Khochfar S., Silk J., 2011, MNRAS, 410, L42
Kim J.-H. et al., 2018, MNRAS, 474, 4232
Kimm T., Cen R., 2014, ApJ, 788, 121
Kovács A., Chapman S. C., Dowell C. D., Blain A. W., Ivison R. J., Smail I., Phillips T. G., 2006, ApJ, 650, 592
Laor A., Draine B. T., 1993, ApJ, 402, 441
Laporte N. et al., 2017, ApJ, 837, L21
Leitet E., Bergvall N., Piskunov N., Andersson B.-G., 2011, A&A, 532, A107
Leitet E., Bergvall N., Hayes M., Linné S., Zackrisson E., 2013, A&A, 553, A106
Li Y. et al., 2008, ApJ, 678, 41
Ma X., Kasen D., Hopkins P. F., Faucher-Giguère C.-A., Quataert E., Kereš D., Murray N., 2015, MNRAS, 453, 960
Ma X., Hopkins P. F., Kasen D., Quataert E., Faucher-Giguère C.-A., Kereš D., Murray N., Strom A., 2016, MNRAS, 459, 3614
Ma X. et al., 2018a, MNRAS, 477, 219
Ma X. et al., 2018b, MNRAS, 478, 1694
Ma X. et al., 2019, MNRAS, 487, 1844
Maio U., Khochfar S., Johnson J. L., Ciardi B., 2011, MNRAS, 414, 1145
Maiolino R., Schneider R., Oliva E., Bianchi S., Ferrara A., Mannucci F., Pedani M., Roca Sogorb M., 2004, Nature, 431, 533
Marrone D. P. et al., 2018, Nature, 553, 51
McKee C. F., Ostriker J. P., 1977, ApJ, 218, 148
McKinnon R., Vogelsberger M., Torrey P., Marinacci F., Kannan R., 2018, MNRAS, 478, 2851
McLure R. J. et al., 2013, MNRAS, 432, 2696
Meurer G. R., Heckman T. M., Calzetti D., 1999, ApJ, 521, 64
Micheva G., Iwata I., Inoue A. K., Matsuda Y., Yamada T., Hayashino T., 2017, MNRAS, 465, 316
Mostardi R. E., Shapley A. E., Steidel C. C., Trainor R. F., Reddy N. A., Siana B., 2015, ApJ, 810, 107
Mo H. J., Mao S., White S. D. M., 1998, MNRAS, 295, 319
Nagamine K., Wolfe A. M., Hernquist L., 2006, ApJ, 647, 60
Narayanan D., Conroy C., Dave R., Johnson B., Popping G., 2018, ApJ, 869, 70
Nozawa T., Kozasa T., Habe A., Dwek E., Umeda H., Tominaga N., Maeda K., Nomoto K., 2007, ApJ, 666, 955
Oesch P. A. et al., 2016, ApJ, 819, 129
Okamoto T., Shimizu I., Yoshida N., 2014, PASJ, 66, 70
Ono Y. et al., 2012, ApJ, 744, 83
Ono Y. et al., 2018, PASJ, 70, S10
Ouchi M., Yamada T., Kawai H., Ohta K., 1999, ApJ, 517, L19
Ouchi M. et al., 2003, ApJ, 582, 60
Ouchi M. et al., 2009, ApJ, 706, 1136
Ouchi M. et al., 2010, ApJ, 723, 869
Paardekooper J.-P., Khochfar S., Dalla Vecchia C., 2013, MNRAS, 429, L94
Paardekooper J.-P., Khochfar S., Dalla Vecchia C., 2015, MNRAS, 451, 2544
Pillepich A. et al., 2018, MNRAS, 475, 648
Ricotti M., Parry O. H., Gnedin N. Y., 2016, ApJ, 831, 204
Riechers D. A. et al., 2013, Nature, 496, 329
Safranek-Shrader C., Agarwal M., Federrath C., Dubey A., Milosavljević M., Bromm V., 2012, MNRAS, 426, 1159
Scannapieco C., Tissera P. B., White S. D. M., Springel V., 2008, MNRAS, 389, 1137
Schaye J., Dalla Vecchia C., 2008, MNRAS, 383, 1210
Schaye J. et al., 2010, MNRAS, 402, 1536
Schaye J. et al., 2015, MNRAS, 446, 521
Schneider R., Omukai K., Inoue A. K., Ferrara A., 2006, MNRAS, 369, 1437
Shapley A. E., Steidel C. C., Pettini M., Adelberger K. L., 2003, ApJ, 588, 65
Sheth R. K., Tormen G., 2002, MNRAS, 329, 61
Shibuya T., Kashikawa N., Ota K., Iye M., Ouchi M., Furusawa H., Shimasaku K., Hattori T., 2012, ApJ, 752, 114
Shimasaku K. et al., 2006, PASJ, 58, 313
Siana B. et al., 2007, ApJ, 668, 62
Silk J., 2013, ApJ, 772, 112
Solomon P. M., Rivolo A. R., Barrett J., Yahil A., 1987, ApJ, 319, 730
Springel V., 2005, MNRAS, 364, 1105
Springel V., Hernquist L., 2003, MNRAS, 339, 289
Springel V., White S. D. M., Tormen G., Kauffmann G., 2001, MNRAS, 328, 726
Steidel C. C., Giavalisco M., Dickinson M., Adelberger K. L., 1996, AJ, 112, 352
Steidel C. C., Pettini M., Adelberger K. L., 2001, ApJ, 546, 665
Steidel C. C., Adelberger K. L., Shapley A. E., Pettini M., Dickinson M., Giavalisco M., 2003, ApJ, 592, 728
Tacconi L. J. et al., 2013, ApJ, 768, 74
Tamura Y. et al., 2019, ApJ, 874, 27
Todini P., Ferrara A., 2001, MNRAS, 325, 726
Trebitsch M., Blaizot J., Rosdahl J., Devriendt J., Slyz A., 2017, MNRAS, 470, 224
Vanzella E. et al., 2012, ApJ, 751, 70
Vanzella E. et al., 2015, A&A, 576, A116
Vanzella E. et al., 2016, ApJ, 825, 41
Vasei K. et al., 2016, ApJ, 831, 38
Watson D., Christensen L., Knudsen K. K., Richard J., Gallazzi A., Michałowski M. J., 2015, Nature, 519, 327
Weingartner J. C., Draine B. T., 2001, ApJ, 548, 296
Wilkins S. M., Feng Y., Di-Matteo T., Croft R., Stanway E. R., Bunker A., Waters D., Lovell C., 2016, MNRAS, 460, 3170
Wise J. H., Turk M. J., Norman M. L., Abel T., 2012, ApJ, 745, 50
Wyithe J. S. B., Loeb A., 2011, MNRAS, 413, L38
Yajima H., Choi J.-H., Nagamine K., 2011, MNRAS, 412, 411
Yajima H., Choi J.-H., Nagamine K., 2012, MNRAS, 427, 2889

Yajima H., Li Y., Zhu Q., Abel T., Gronwall C., Ciardullo R., 2014a, MNRAS, 440, 776
Yajima H., Nagamine K., Thompson R., Choi J.-H., 2014b, MNRAS, 439, 3073
Yajima H., Li Y., Zhu Q., Abel T., 2015a, ApJ, 801, 52
Yajima H., Shlosman I., Romano-Díaz E., Nagamine K., 2015b, MNRAS, 451, 418
Yajima H., Nagamine K., Zhu Q., Khochfar S., Dalla Vecchia C., 2017a, ApJ, 846, 30
Yajima H., Ricotti M., Park K., Sugimura K., 2017b, ApJ, 846, 3
Yajima H., Sugimura K., Hasegawa K., 2018, MNRAS, 477, 5406
Yang M., Greve T. R., Dowell C. D., Borys C., 2007, ApJ, 660, 1198
Younger J. D. et al., 2009, ApJ, 704, 803
Zavala J., Okamoto T., Frenk C. S., 2008, MNRAS, 387, 364

This paper has been typeset from a TEX/LATEX file prepared by the author.